The Astrophysical Journal, 949:97 (23pp), 2023 June 1 https://doi.org/10.3847/1538-4357/acce3f

Investigating the Time Evolution of the Thermal Emission from the Putative Neutron Star in SN 1987A for 50+ Years

Akira Dohi[1,2], Emanuele Greco[3,4,5,6], Shigehiro Nagataki[2,7,8], Masaomi Ono[2,7,9], Marco Miceli[5,6], Salvatore Orlando[5], and Barbara Olmi[5]
[1] Department of Physics, Kyushu University, Fukuoka 819-0395, Japan; akira.dohi@riken.jp
[2] RIKEN Interdisciplinary Theoretical and Mathematical Sciences Program (iTHEMS), 2-1 Hirosawa, Wako, Saitama 351-0198, Japan
[3] Anton Pannekoek Institute for Astronomy, University of Amsterdam, Science Park 904, 1098 XH Amsterdam, The Netherlands
[4] GRAPPA, University of Amsterdam, Science Park 904, 1098 XH Amsterdam, The Netherlands
[5] INAF-Osservatorio Astronomico di Palermo, Piazza del Parlamento 1, I-90134 Palermo, Italy
[6] Università degli Studi di Palermo, Dipartimento di Fisica e Chimica, Piazza del Parlamento 1, I-90134 Palermo, Italy
[7] Astrophysical Big Bang Laboratory (ABBL), RIKEN Cluster for Pioneering Research, 2-1 Hirosawa, Wako, Saitama 351-0198, Japan
[8] Astrophysical Big Bang Group (ABBG), Okinawa Institute of Science and Technology Graduate University, 1919-1 Tancha, Onna-son, Kunigami-gun, Okinawa 904-0495, Japan
[9] Institute of Astronomy and Astrophysics, Academia Sinica, Taipei 10617, Taiwan
Received 2022 August 1; revised 2023 March 12; accepted 2023 April 13; published 2023 June 2

Abstract

Observations collected with the Atacama Large Millimeter/submillimeter Array (ALMA) and analysis of broadband X-ray spectra have recently suggested the presence of a central compact object (CCO) in SN 1987A. However, no direct evidence of the CCO has been found yet. Here we analyze Chandra X-ray observations of SN 1987A collected in 2007 and 2018, and synthesize 2027 Chandra and 2037 Lynx spectra of the faint inner region of SN 1987A. We estimate the temporal evolution of the upper limits of the intrinsic luminosity of the putative CCO in three epochs (2018, 2027, and 2037). We find that these upper limits are higher for higher neutron star (NS) kick velocities due to increased absorption from the surrounding cold ejecta. We compare NS cooling models with both the intrinsic luminosity limits obtained from the X-ray spectra and the ALMA constraints with the assumption that the observed blob of SN 1987A is primarily heated by thermal emission. We find that the synthetic Lynx spectra are crucial to constrain the physical properties of the CCO, which will be confirmed by future observations in the 2040s. We draw our conclusions based on two scenarios, namely the nondetection and detection of the NS by Lynx. If the NS is not detected, its kick velocity should be $\simeq$700 km s^{-1}. Furthermore, nondetection of the NS would suggest rapid cooling processes at the age of 40 yr, implying strong crust superfluidity. Conversely, in the case of NS detection, the mass of the NS envelope must be high.

Unified Astronomy Thesaurus concepts: Supernovae (1668); Neutron stars (1108); Supernova remnants (1667); Compact objects (288); X-ray astronomy (1810); X-ray sources (1822)

1. Introduction

The explosion of the core-collapse supernova (SN) 1987A, which was confirmed through the detection of neutrinos on 1987 February 23 (Hirata et al. 1987; Bionta et al. 1987), is of great importance for understanding the physics of young central compact objects (CCOs). However, there has been no direct detection of the CCO of SN 1987A yet. With recent observational progresses, the first hints of CCO emission have been reported by Atacama Large Millimeter/submillimeter Array (ALMA) observations (Cigan et al. 2019). The authors suggested the existence of a warm dust blob hiding the CCO with (40–90) $L_\odot$. For an explanation of the observed luminosity, several mechanisms have been argued, such as heating by the radioactive decay of ^{44}Ti, magnetospherically powered emission from the spin down of a young pulsar, accretion-powered heating, and thermal (blackbody) emission from the CCO (see also Table 1 in Page et al. 2020). Thus, further investigation is needed in order to clarify the origin of the observed excess in the luminosity and therefore, potentially to identify the CCO emission.

Page et al. (2020) investigated the thermal emission scenario with their neutron star (NS) cooling models, concluding that thermal emissions from the CCO could reproduce the observed excess luminosity. Hence, multiwavelength observations of SN 1987A can probe the NS model parameters, such as envelope properties, equation of state (EOS), the NS mass, and nucleon superfluid/superconductive models. They suggested that consistent cooling models of the possible NS in SN 1987A (NS 1987A hereafter) must have many light elements on the surface; the corresponding envelope mass is $M_{\rm env} \gtrsim 10^{-9}\,M_\odot$.[10] They also mentioned that the superfluidity in the $^1S_0$ state of neutrons in the crust may be weak in a certain range of $M_{\rm env}$ (see their Figure C1). Thus, the information of SN 1987A helps to constrain the NS models, which have still been uncertain despite several recent experiments and observations

[10] Assuming that the degenerated electrons are dominant for supporting the outer crust and all nuclei are symmetric, one can get a relation (e.g., Beznogov et al. 2021):

$$M_{\rm env} = 1.9 \times 10^{-9} \rho_8 g_{s,14}^{-2} M_{\rm NS}, \quad (1)$$

where $M_{\rm NS}$ is the NS mass in units of $M_\odot$, $g_{s,14}$ is the surface gravity normalized by 10^{14} cm s^{-2}, and ρ_8 is the maximum density reached by the light elements in the crust normalized by 10^8 g cm^{-3}. The thermal emission scenario requires $\rho_8 \gtrsim 1$ for the ALMA observations of SN 1987A (Page et al. 2020), implying $M_{\rm env} \gtrsim 1.2 \times 10^{-9}\,M_\odot$ for canonical NSs with $M_{\rm NS} = 1.4\,M_\odot$ and a radius of 12 km.

(e.g., Lattimer & Prakash 2016; Özel & Freire 2016; for more recent constraints, see Sotani et al. 2022 and reference therein.).

The thermal luminosity from an NS can be calculated from NS cooling theories, which describe how the NS cools down after its birth, mainly by neutrino losses (at ages $t \lesssim 10^5$ yr), because their mean free path is larger than the NS radius (Shapiro & Teukolsky 1983). Neutrinos are produced by many kinds of particle reactions inside the NS, e.g., modified/direct Urca (DU) processes, bremsstrahlung, and pair breaking and formation (PBF) in nucleon superfluid states. Hence, the time evolution of the thermal luminosity, which we call the cooling curve, is affected by the interior NS properties. Moreover, the envelope also affects the thermal luminosity through the thermal/electron conductivities and possible accretion and nuclear heating (for a review, see Beznogov et al. 2021). Many works have investigated the complex behaviors of cooling curves to explain many temperature observations of NSs (for reviews, see, e.g., Yakovlev & Pethick 2004; Page et al. 2006). In particular, the young NS of Cassiopeia A (∼340 yr) is the first observational target to test the cooling theories for an early phase, and the modeling has been very successful, indicating strong neutron superfluidity in the core ($T_{\rm cr,peak} \sim$ (5–6) $\times 10^8$ K, where $T_{\rm cr,peak}$ is the maximum superfluid transition temperature in all-density regions; Page et al. 2011; Shternin et al. 2011). While Cassiopeia A observations allow us to extract information on the superfluidity in the core, NS 1987A would provide relevant hints about the superfluidity in the crust, assuming thermal emission of the NS as the origin of the observed excess in the ALMA observation. This is because of the difference of the thermal relaxation time (t_w) when the heat in the crust or core is completely transported to the surface, which is typically $t_w \gtrsim 100$ yr for the heat in the core while $t_w \lesssim 100$ yr in the crust (Lattimer et al. 1994; Gnedin et al. 2001; Sales et al. 2020). Therefore, NS 1987A is one of the few candidates to probe crust superfluidity, which is still unclear (but see also the recent study of ultracold atomic gases by Tajima et al. 2019).

X-ray observations provide beneficial information of NS 1987A. For example, Greco et al. (2021) analyzed Chandra and NuSTAR observations of SN 1987A and suggested that the spectra could be better explained by including a nonthermal component. The nonthermal component is most likely arising from a pulsar wind nebula (PWN; but see also Alp et al. 2021). This scenario is further investigated by a recent follow-up paper (Greco et al. 2022), which also provides additional information on the putative NS spin period and time derivative. Thus, although direct X-ray observations of the NS 1987A have not been successful made yet, our understanding of the properties of the NS continues to improve.

Even in the case of the nondetection of the CCO, X-ray observations of SN 1987A can however provide upper limits for the thermal luminosity, which provide us with information of NS 1987A. Actually, Shternin & Yakovlev (2008) investigated consistent cooling models of NS 1987A with Chandra, XMM-NEWTON, and INTEGRAL observations around 2000, which show $L^{\infty}_{\gamma,35} \lesssim 0.2$, where $L^{\infty}_{\gamma,35}$ is the redshifted photon luminosity in units of 10^{35} erg s^{-1}. They concluded that such an upper limit for NS 1987A requires distinctive physical factors to cool around $t \simeq 13$ yr, such as strong crust superfluidity. In this work, we similarly constrain the cooling curves by considering both ALMA and recent X-ray observations. Regarding the ALMA constraints, we assume that the CCO is an NS emitting thermal emission with $L^{\infty}_{\gamma,35} \sim 1$, which is responsible for the heating of the observed blob, i.e., the thermal emission scenario (see Section 4 for details). We also investigate future upper limits on the luminosity of the X-ray thermal emission, based on synthetic Chandra and Lynx spectra, exploiting the diagnostic power provided by the state-of-the-art magnetohydrodynamics (MHD) simulation of SN 1987A by Orlando et al. (2020).

This paper is organized as follows. In Section 2, we describe the details of the analysis of recent Chandra observations, and we present upper limits on the intrinsic luminosity of the NS. In Section 3, we summarize the information of our NS cooling models, which include neutrino and photon cooling processes, superfluid models, and envelope models. In Section 4, we present our cooling models and compare them with ALMA, Chandra, and Lynx (future) observations. Then, we discuss the two cases of nondetection and detection of the CCO in the 2040s by a predicted future Lynx X-ray observation. We finally give concluding remarks in Section 5.

2. Analysis of the Chandra Observations of SN 1987A

Considering the young age of the system and the expected NS kick velocity of roughly 300–700 km s^{-1} (see Cigan et al. 2019; Orlando et al. 2020), we expect that the CCO lies in the internal area of SN 1987A, within a radius of ∼0.″5 and the Chandra/ACIS charge-coupled device (CCD) is the only X-ray detector currently able to resolve it spatially. In this paper, we consider 27 different Chandra observations performed in 2007 and 2018. We summarize the main information of all the observations in Table 1.

2.1. Data Reduction

We reduce the data following the standard procedure within the CIAO software, version 4.12 with CALDB 4.9.2.1, through the task `chandra_repro` (Fruscione et al. 2006). We merge observations performed in the same year (2007 and 2018) with `merge_obs` to produce count-rate images of SN 1987A in the broad 0.5–7 keV band (upper panels of Figure 1). We deconvolve the resulting images by the Chandra/ACIS-S point-spread-function (PSF) with the Lucy algorithm (Lucy 1974; Richardson 1972) through the `arestore` task (lower panels of Figure 1). We considered a convergence criterion based on the self-similarity of the images after a given number of iterations, equal to 50 in our case.

The putative NS is expected to have a kick velocity (Orlando et al. 2020) which, projected on the plane of the sky, typically is $\lesssim$2000 km s^{-1} (Hobbs et al. 2005; Katsuda et al. 2018). Therefore, we select a 0.″3 radius circle from the deconvolved count-rate maps and consider this as the region in which to look for possible radiation from the NS, as done by Esposito et al. (2018). The resulting source and background regions used for spectral extraction are shown in Figure 1 in white and red, respectively.

We extract the Chandra spectra from each observation with the `specextract` tool within CIAO. The resulting spectra show <100 counts. To improve the spectral statistics, we combine all the spectra and the corresponding response and background files collected in the same epoch through the HEAsoft task `addascaspec`, achieving reasonable error bars and binning. The corresponding combined response file is obtained by properly averaging between all the response files. This choice is justified by the small time range in which the

Table 1
Main Characteristics of the Chandra Observations

Date	ObsID	PI	Exposure Time (ks)
2007/03/11	8523	Canizares	30
2007/03/12	8537	Canizares	13
2007/03/13	7588	Canizares	27
2007/03/18	8538	Canizares	21
2007/03/19	7589	Canizares	25
2007/03/20	8539	Canizares	25
2007/03/21	8542	Canizares	18
2007/03/24	8487	Canizares	29
2007/03/27	8543	Canizares	31
2007/03/28	8544	Canizares	19
2007/03/29	8488	Canizares	32
2007/03/31	8545	Canizares	20
2007/04/01	8546	Canizares	31
2007/04/17	7590	Canizares	35
	Total 2007		338
2018/03/14	20927	Park	17
2018/03/15	21037	Park	30
2018/03/18	21038	Park	34
2018/03/19	20322	Park	15
2018/03/23	21042	Park	41
2018/03/25	21043	Park	29
2018/03/26	21044	Park	15
2018/03/27	20323	Park	27
2018/03/28	21049	Park	31
2018/03/29	21050	Park	18
2018/03/30	21051	Park	15
2018/03/31	21052	Park	30
2018/04/02	21053	Park	12
	Total 2018		314

coeval observations are performed, ∼15 days. Thanks to this approach, we obtain a unique spectrum for each epoch, with $\gtrsim$1000 counts. The combined 2007 and 2018 spectra are then rebinned to 25 counts per bin.

2.2. Spectral Analysis

We fit the combined spectra by adopting a model including a foreground absorption component (`TBabs` model in XSPEC; Arnaud 1996), and an optically thin isothermal component emitting in nonequilibrium of ionization (`vnei` model in XSPEC). In the following, we refer to this `TBabs*vnei` model as the 1-nei model. The total column density $N_{\rm H}$[11] is fixed to 2.35×10^{21} cm^{-2} (Park et al. 2006). The temperature, emission measure, ionization parameter, and the plasma metallicity are left free to vary.

By adopting the 1-nei model, we obtain a $\chi^2 = 47.98$ with 31 degrees of freedom (d.o.f.) in 2007 and a $\chi^2 = 49.98$ with 44 d.o.f. in 2018. Subsequently, we add another `vnei` component, which we refer to this `TBabs*(vnei+vnei)` as the 2-nei model. Then, we obtain an improvement in the fit quality, achieving $\Delta\chi^2 = -15$ in 2007 and $\Delta\chi^2 = -17$ in 2018 with three additional parameters. In this 2-nei model scenario, we force the metallicities of the two components to be equal. We note that in both the models the ionization age τ is poorly constrained. This is an effect of the low statistics of the spectra. In any case, as discussed in the next subsection, our results do not depend on this particular value. The 2007 and 2018 Chandra spectra with the corresponding best-fit model and residuals are shown in Figure 2. Details of the best-fit parameters are shown in Table 2.

[11] Strictly speaking, this is an "equivalent average" column density assuming Milky Way interstellar medium abundances, to have two different absorption components with Galactic and LMC abundances, respectively.

2.3. Absorption from Cold Ejecta

To estimate the absorption pattern due to the cold ejecta, we exploit the MHD simulation of SN 1987A from Orlando et al. (2020). The complete details of the procedure we adopted to model the X-ray absorption form the cold ejecta are given in Appendix B of Greco et al. (2021) and in Section 2.1 of Greco et al. (2022), thus here we only recall the main steps. The values of the temperature, density, chemical composition, and ionization age of the plasma are associated with each cell of the 3D spatial domain of the MHD model. We extract the ionic density, chemical abundances, and electronic temperature from each cell of the 3D domain and include them in the spectral analysis through the `vphabs` component available in XSPEC, which provides the absorbing power due to the photoelectric effect. We repeat the procedure for every year considered in this work (2007, 2018, 2027, and 2037), also taking into account the proper motion of the putative CCO, whose kick velocity is provided by the MHD model under the assumption of momentum conservation (see Ono et al. 2020 for details). We consider the modulus of the kick velocity, $v_{\rm kick} = 300$ km s^{-1}, provided by the model as a lower limit (Orlando et al. 2020). Moreover, from an analysis of the ALMA observation, Cigan et al. (2019) measured an offset between a dust blob (possibly related to the NS) and the location of the progenitor star estimated by Alp et al. (2018), and derived an upper limit to the kick velocity of 700 km s^{-1}. To maintain our analysis as general as possible, we estimate the ejecta absorbing power by assuming three possible kick velocities: 300, 500, and 700 km s^{-1}.

We note that the three different kick velocities imply different linear momenta of the NS. Consequently, a different distribution of the ejecta for the three cases should be expected on the basis of the conservation of momentum. On the other hand, the linear momentum of the NS reflects the total linear momentum of the ejecta, i.e., the difference between the linear momenta of the two portions of the ejecta that propagate in the two opposite directions defined by the bipolar SN explosion assumed in the model of SN 1987A. This difference is much smaller (by a factor of 20) than each of the momentum of these two portions of ejecta. An increase of a factor of two in the linear momentum of the NS (corresponding to increasing its kick velocity by a factor of two) would imply very small changes in the total ejecta distribution. In light of this, we considered the NS kick velocity calculated from the model on the basis of exact momentum conservation (∼300 km s^{-1}) and explored the possibility of higher kick velocities up to the value estimated by (Cigan et al. 2019; namely 700 km s^{-1}) without the need to run new MHD simulations (which would require a very high computational cost).

We built a map (Figure 3) showing the bolometric emerging flux in the northeastern region of SN 1987A, where the NS is expected to be according to the MHD model. The remnant is oriented according to the inclination of the dense equatorial ring, as found from an analysis of optical data (e.g., Sugerman et al. 2005). To each pixel of Figure 3 is associated a value of flux, expressed in erg s^{-1} cm^{-2}, estimated by convolving the redshifted emission irradiated by a 11.57 km radius and 1.4 $M_\odot$ NS with ejecta absorption. Since the density and the chemical

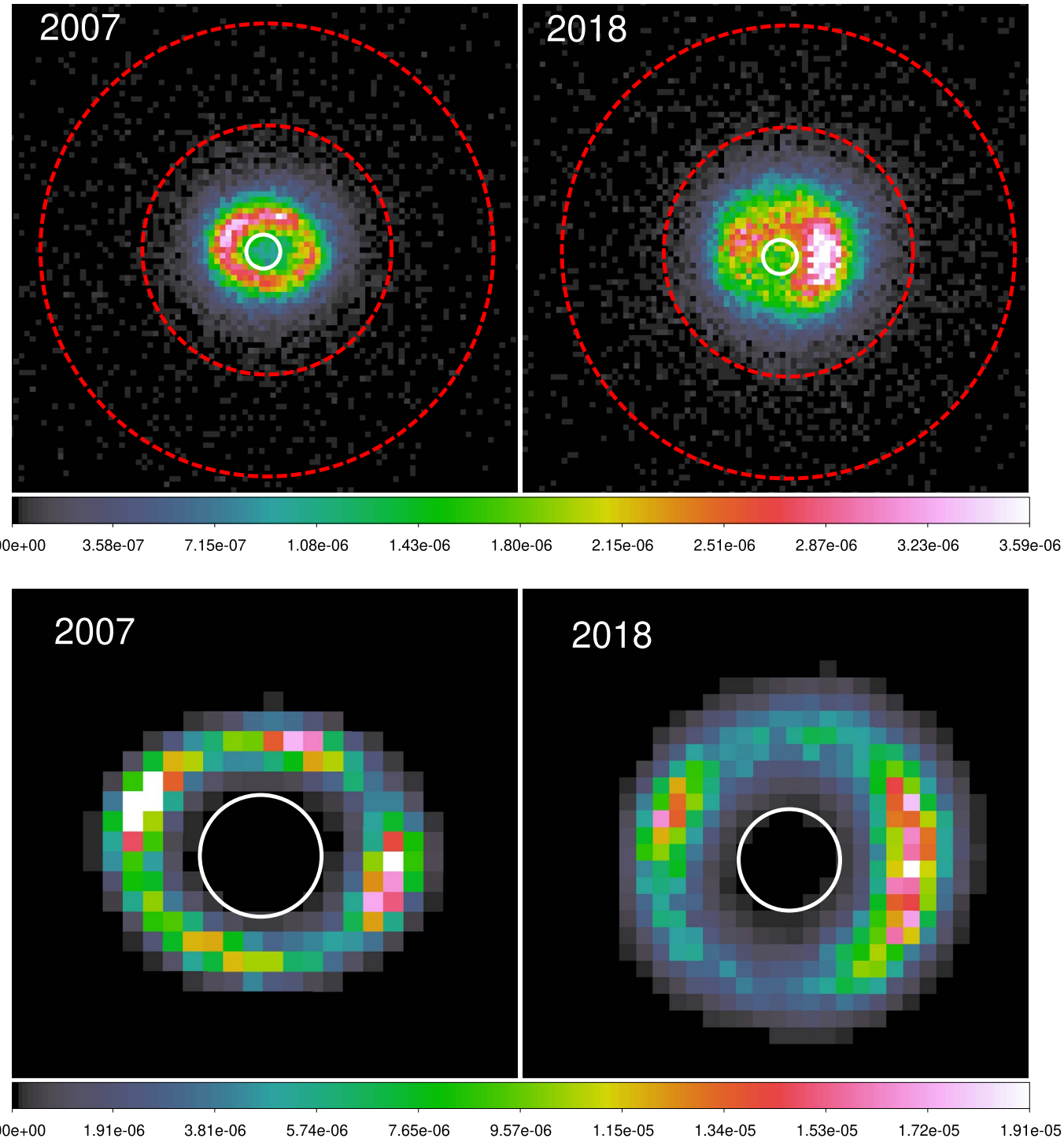

Figure 1. Broad (0.5–7 keV) Chandra/ACIS-S exposure-corrected count-rate maps of SN 1987A in 2007 and 2018, using subpixel sampling (bin size of 0.″1). Upper panels: source and background regions are shown in white and dashed red, respectively. Lower panels: same as the upper panels but the count-rate maps are deconvolved by the Chandra PSF through the Lucy algorithm.

distribution change pixel by pixel, the corresponding emerging flux varies accordingly. In particular, darker areas mark lower emerging flux and, subsequently, higher ejecta absorbing power. Red, orange, and yellow dots show the position of the putative NS assuming a kick velocity of 300 km s^{-1}, 500 km s^{-1}, and 700 km s^{-1}, respectively. The figure also shows cyan contours corresponding to the 679 GHz dust emission at 3σ and 5σ reported in Figure 3 of Cigan et al. (2019), which are in good agreement with the findings in this paper. Figure 3 clearly shows that considering a higher kick velocity leads to an NS embedded in more effectively absorbing material, with the peak of the absorption corresponding to a shell at $\sim$0.″1 from the center of the explosion.

2.4. Upper Limits of the Bolometric Redshifted Luminosity

We include in our model a `bbodyrad` component to look for thermal (blackbody) radiation stemming from the putative NS. Two effects influence the blackbody spectral shape: (i) the gravitational redshift z and (ii) absorption from

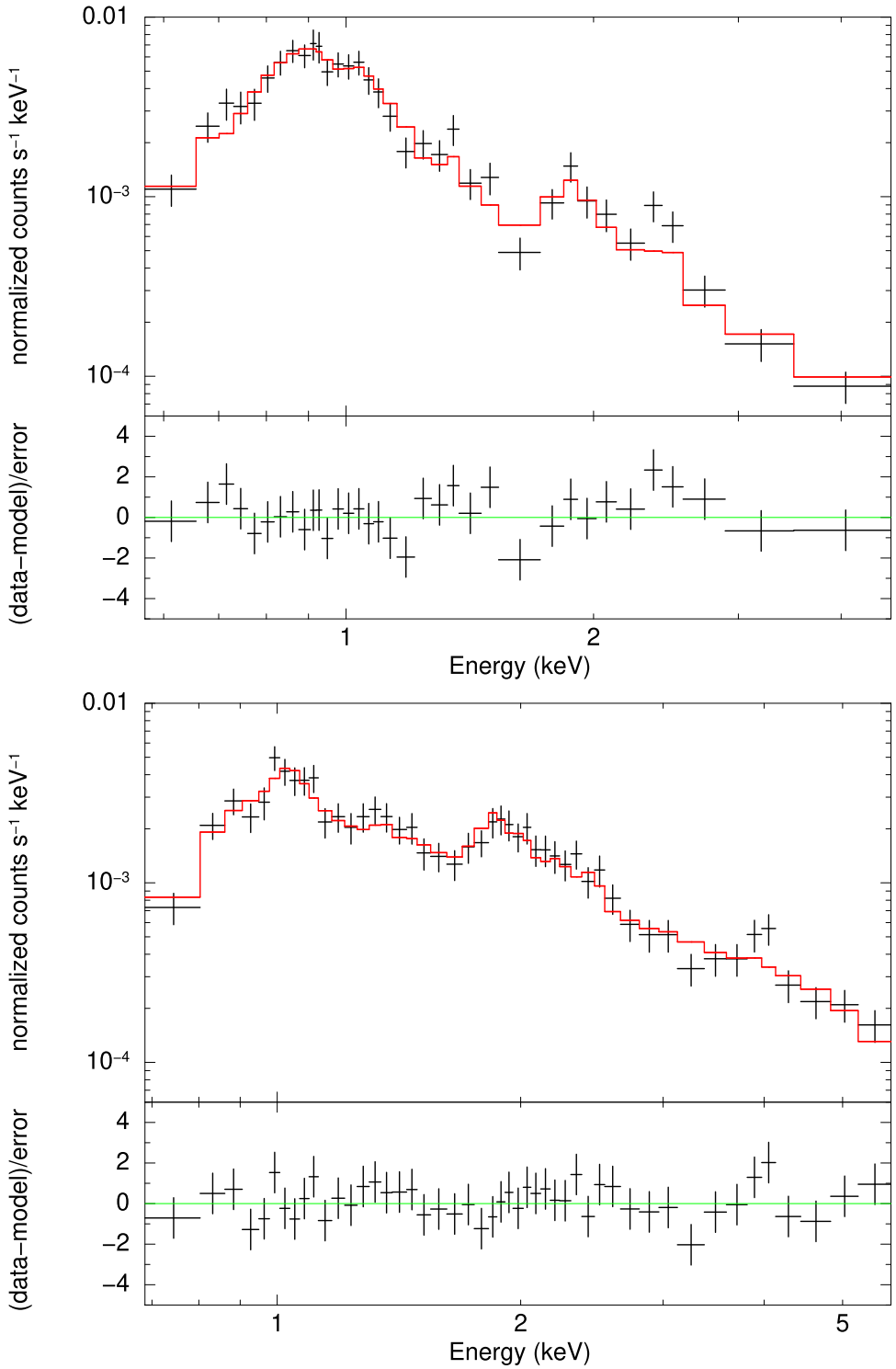

Figure 2. Combined Chandra/ACIS-S spectra (in black) extracted from the inner region of SN 1987A (shown in white in Figure 1), with the corresponding best-fit model (in red) and residuals (bottom window of each panel). Data from 2007 and 2018 are shown, respectively, in the upper and bottom panels.

the interstellar medium along the line of sight and from the inner ejecta lying in the very heart of SN 1987A. Besides, the model of the NS atmosphere also changes the spectral shape through radiative thermal conductivity, which is explained in Section 3. The gravitational redshift can be estimated given the radius and the mass of the NS. Foreground absorption from the interstellar medium is already included in our model with the `Tbabs` component as fixed to be $N_H = 2.35 \times 10^{21}$ cm^2 (Park et al. 2006). The absorption due to the inner ejecta requires a bit more effort and it is extensively discussed in Section 2.3.

We add the absorbed and redshifted blackbody spectrum to our 2-nei model in both years. In the following, we refer to this model as the *bb model*.[12] Since the characteristic dimension of

[12] In XSPEC terms, this model reads as `TBabs*(vnei+vnei+vphabs (zashift(bbodyrad)))`. Note that the order of `vphabs` and `zashift` matters, since the blackbody radiation is first redshifted and then absorbed.

Table 2
Best-fit Parameters of the 2007 and 2018 Spectra

Parameter	2007		2018	
	1-nei model	2-nei model	1-nei model	2-nei model
N_H (10^{21} cm^{-2})		2.35 (fixed)		
kT_1 (keV)	$0.81^{+0.26}_{-0.16}$	$0.81^{+0.26}_{-0.16}$	$1.9^{+0.3}_{-0.2}$	$0.7^{+0.2}_{-0.3}$
Abundance$_1$	$0.30^{+0.13}_{-0.09}$	$0.9^{+1.6}_{-0.3}$	$0.19^{+0.07}_{-0.05}$	$0.24^{+0.16}_{-0.10}$
τ_1 (10^{11} s cm^{-3})	$3.8^{+1.3}_{-0.8}$	0.9 ± 0.4	$0.41^{+0.15}_{-0.10}$	>1
Emission measure$_1$ (10^{58} cm^{-3})	$0.52^{+0.21}_{-0.15}$	$0.23^{+0.37}_{-0.14}$	1.1 ± 0.2	1.0 ± 0.6
kT_2 (keV)	/	$1.9^{+2.2}_{-0.5}$	/	$2.6^{+0.9}_{-0.5}$
Abundance$_2$	/	=Abundance$_1$	/	=Abundance$_1$
τ_2 (10^{11} s cm^{-3})	/	>1	/	$0.8^{+0.5}_{-0.3}$
Emission measure$_2$ (10^{58} cm^{-3})	/	$0.23^{+0.3}_{-0.11}$	/	$0.6^{+0.3}_{-0.2}$
χ^2 (d.o.f.)	47.98 (31)	32.78 (28)	49.98 (44)	32.99 (41)

Note. Error bars are at 90% confidence level.

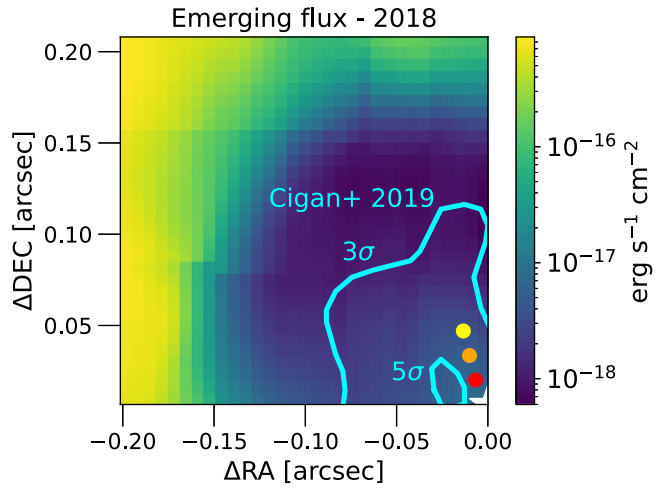

Figure 3. Map of the emerging flux for the year 2018. The origin is set at the assumed center of explosion (bottom right corner). Red, orange, and yellow dots indicate the position of the putative NS assuming the direction of the kick according to the MHD model of Orlando et al. (2020) and a kick velocity of 300 km s^{-1}, 500 km s^{-1}, and 700 km s^{-1}, respectively. Cyan contours trace the 679 GHz dust emission at 3σ and 5σ, as reported in Figure 3 of Cigan et al. (2019).

the inner region of SN 1987A is smaller than the Chandra PSF, we correct the normalization of the `bbodyrad` component to take into account the fractional encircled energy (see Figure 4.6 on the Chandra OG website). In our case, the peak of the absorbed blackbody is at roughly 4 keV, which, for a region with a radius of 0.″3, requires a correction factor $f_{PSF} \sim 0.5$. Therefore, we correct the normalization of the `bbodyrad` component by f_{PSF} before translating its best-fit value into the radius of the NS.

All the parameters relative to the redshift and ejecta absorption components are kept frozen during the fitting procedure. We find no significant improvement in the description of the data with this *bb model*, even by considering different kick velocities and/or masses of the NS, indicating that there is no evidence for any thermal emission stemming from the NS. Given the nondetection of the NS radiation, we can only put upper limits on its flux. The most constraining upper limits come from the 2018 data, since the absorbing power of the cold ejecta decreases with time due to their expansion (see Greco et al. 2022 for a public repository of the absorption components from 2001 to 2037). Therefore, in the following, we focus on these more recent data sets.

As mentioned above, fitting the data with the 2-nei model or the *bb model* leads to identical values of χ^2. To investigate the upper limit on the luminosity of the putative NS we estimate the maximum blackbody luminosity compatible with the observed spectrum at 90% (1.6σ) and 99.7% (3σ) confidence levels. We adopt the following approach: we fix all the parameters corresponding to the emission of the NS, i.e., the redshift, the normalization, and the temperature; we fix the mass and the radius of the emitting blackbody; we keep free to vary all the parameters of the 2-nei components, as shown in Table 2; and we fit the data by increasing the temperature of the blackbody until $\Delta\chi^2 = 2.706$ or $\Delta\chi^2 = 9$ is achieved, evaluated with respect to the best-fit 2-nei model. With this approach, we obtain the maximum temperature allowed for the given configuration of the *bb model*. Since the luminosity of a blackbody, at a fixed radius, depends only on the temperature we also infer the upper limits of the bolometric redshifted luminosity of the NS. We repeat this procedure for the three kick velocities (300, 500, and 700 km s^{-1}) and three masses (1.2 $M_\odot$, 1.4 $M_\odot$, and 1.6 $M_\odot$) of the NS. The resulting 2018 upper limits are shown in the Appendix.

The 2018 upper limits we find are in good agreement with the ones reported by Alp et al. (2018). However, as we show in the next sections, these values do not allow us to exclude any of the possible cooling curves relative to the thermal emission of the putative NS. Therefore, we investigate how the luminosity upper limit would change in the upcoming years. Since the absorbing power of the ejecta decreases with time, we expect the luminosity upper limit to decrease as well.

We need to synthesize reliable future X-ray spectra in order to estimate robustly the time variation of the upper limits. The MHD model by Orlando et al. (2020) predicts that the flux arising from the supernova remnant (SNR) in the inner faint area of SN 1987A is constant between 2018 and 2037. Therefore, we synthesized fiducial 2027 Chandra/ACIS-S and 2037 Lynx/X-ray Microcalorimeter (LXM) spectra of the inner area of SN 1987A, starting from the best-fit 2-nei model obtained for the 2018 Chandra/ACIS-S data (Table 2). The luminosity upper limits also depend on the assumed exposure time, since the statistics affect the sensitivity of the spectra to the additional `bbodyrad` component. Therefore, we synthesize the 2027 and 2037 spectra assuming two different

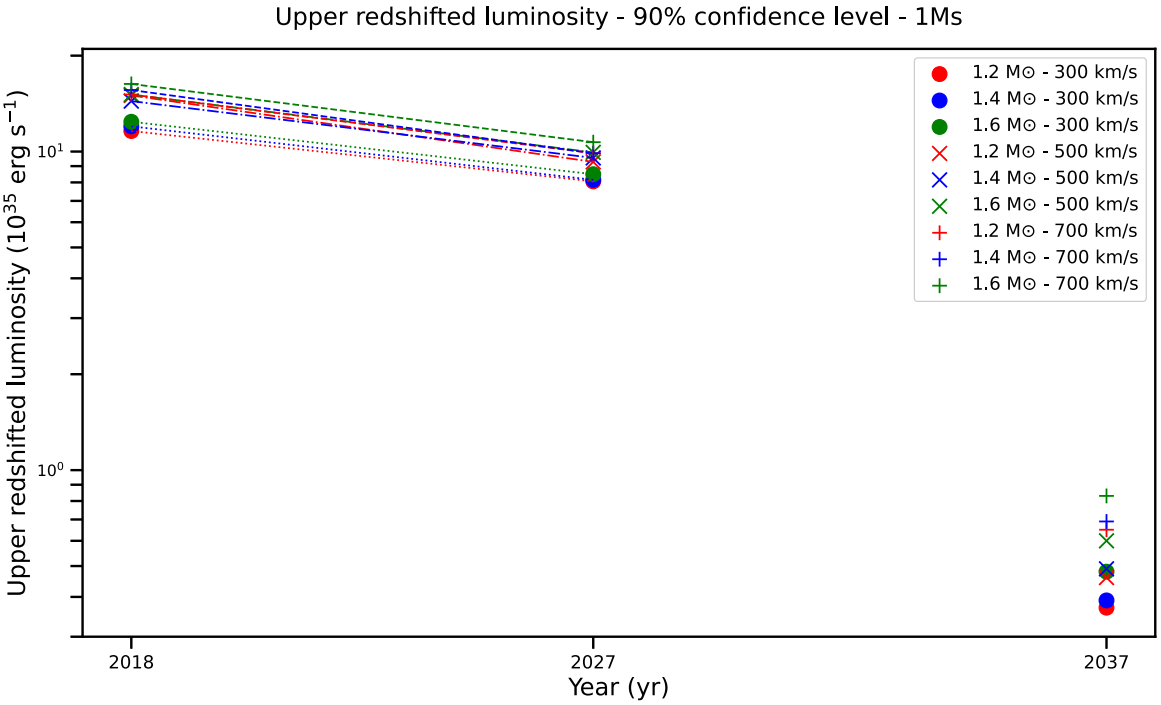

Figure 4. Evolution with time of upper limit of the redshifted (bolometric) luminosity estimated at the 90% confidence level. The synthetic Chandra and Lynx spectra are produced assuming an exposure time of 1 Ms. Colors red, blue, and green indicate an NS mass of 1.2 $M_{\odot}$, 1.4 $M_{\odot}$, and 1.6 $M_{\odot}$, respectively. The circles, crosses, and pluses indicate a kick velocity of 300 km s^{-1}, 500 km s^{-1}, and 700 km s^{-1}, respectively. Upper limits derived from spectra collected with the same instrument (namely Chandra) are linked with lines.

exposure times: 200 ks, similar to the Chandra/ACIS-S observations performed in 2018, and 1 Ms, typical of large program observations. The resulting spectra are then analyzed by following the same procedure described for the 2018 data: we find the 2-nei best-fit model and then we estimate the 90% and 99.7% upper limits on the luminosity through the *bb model*. It is worth noticing that the *bb model* used to fit the synthetic spectrum takes into account the variation of local absorption by the ejecta. The luminosity upper limits for 2027 and the 2040s are shown in the Appendix. It is noted that Lynx will not likely be launched in 2037, but our conclusion is qualitatively unchanged as long as Lynx is launched in the 2040s; see Section 4.3 for details. From such a standpoint, we tentatively label the launched year of Lynx as "2040s", not 2037 as previously stated here.

We show the time evolution of the upper limits at the 90% confidence level, measured from the 1 Ms synthetic spectra, in Figure 4 to highlight the time evolution of these quantities better. Other scenarios considering the 99.7% confidence level and a 200 ks exposure time provide less constraining upper limits and are shown in Appendix (Figures 15, 16, and 17). The time evolution shown in Figure 4 clearly shows a decreasing trend. This is well expected, given that our reference MHD model predicts an expansion of the internal ejecta of SN 1987A, leading to a less efficient photoelectric effect and, finally, to lower upper limits. 1.2 $M_{\odot}$−300 km s^{-1} is the scenario which shows the lowest upper limit, in each of the years considered. This is due both to the cocoon-like distribution of the ejecta, and to the gravitational redshift of the blackbody radiation: lower mass implies lower redshift. Since the X-ray flux due to shock-heated plasma is higher at energies $\lesssim$ 2 keV, the more the blackbody radiation is redshifted, more flux becomes hidden below the observed spectrum. Therefore, the redshift has a more important role than the size of the NS in the upper limit measure, which changes by just a few percent from the scenario with 1.6 $M_{\odot}$ (11.45 km radius) to the 1.2 $M_{\odot}$ one (11.65 km radius).

We also notice a significant decrease (roughly a factor of 30) of the upper limits by Lynx, with respect to Chandra. We find the absorbed flux to increase by a factor of ∼3 in that period, while the additional difference of a factor ∼10 is due to the instrument used for the synthesis of the spectra. In fact, the high sensitivity of the Lynx X-ray microcalorimeter is beneficial to the estimate of the upper limits, since small variations of the *bb model* spectrum lead to a noticeable increase in the $\Delta\chi^2$ value. Subsequently, when Lynx will be operating we will be able to discern better between the various blackbody scenarios even if the CCO will not be detected yet.

Our study of the parameter space of the *bb model* not only provides future upper limits for the bolometric luminosity, but it also may be used as a constraint on the NS or SNR characteristics in the case of a direct detection of the compact object. For instance, if in the 2040s a successful detection of the CCO will be performed, we would have constraints on its kick velocity, mass, or radius.

3. Cooling Models

Thermal evolution of isolated NSs can be divided into two cooling stages: the first period is called the neutrino cooling era, in which neutrino processes working inside NSs are dominant in their thermal evolution. This era lasts until $t \sim 10^5$ yr after the formation of the NS, hence the putative NS 1987A lies in this era. Once the neutrino cooling era is over, the so-called photon cooling era begins, since the neutrino luminosity becomes lower than the photon luminosity due to the low internal temperature of the NS. To describe such a long-term thermal evolution with cooling models properly,

we need a realistic EOS, cooling processes, superfluid/superconductive models, and envelope models.

To describe the NS structure and composition, we adopt the widely used Akmal–Pandharipande–Ravenhall (APR) EOS, which is built based on realistic two-body interaction and phenomenological three-body interaction (Akmal et al. 1998). The maximum mass is $2.183\,M_{\odot}$, which agrees with Shapiro-delay based mass measurements of pulsars (Demorest et al. 2010; Antoniadis et al. 2013; Cromartie et al. 2020). If the proton fraction inside the NS exceeds one-ninth (without muons), the DU process works because of momentum conservation and a rapidly cooling NS, whose threshold central density or mass naturally depends on the EOS (Boguta 1981; Lattimer et al. 1991). In the APR EOS, the threshold mass of the DU process is $1.96\,M_{\odot}$. Since current predictions from observations of light curves of SN 1987A indicate $1.22 \leqslant M_{\rm NS}/M_{\odot} \leqslant 1.62$ (Shigeyama et al. 1988; Woosley 1988; Utrobin et al. 2019; Ertl et al. 2020; Page et al. 2020), in this work we have limited the NS mass to the range 1.2–$1.6\,M_{\odot}$, which then excludes the possibility of having DU processes.

Radii of 11.65, 11.57, and 11.45 km correspond to NSs with masses of 1.2, 1.4, and $1.6\,M_{\odot}$, respectively, coherent with the X-ray analysis described in Section 2. We note that, under such a minimal cooling scenario (Page et al. 2004), the influence of the EOS uncertainties on the cooling curves is not so large compared with other model parameters (e.g., Yakovlev & Pethick 2004; Lim et al. 2017).

In the neutrino cooling era, the neutrino emission processes that dominate in most NSs are so-called slow and medium cooling processes. The latter arises because of nucleon superfluidity. The former mainly includes the modified Urca (MU) process and bremsstrahlung in nucleon–nucleon collisions (Yakovlev & Levenfish 1995). The emissivity of slow cooling processes is approximately expressed as follows:

$$\epsilon_{\nu}^{\rm Slow} \approx 10^{19-21}\left(\frac{\rho_{\rm B}}{\rho_{\rm nuc}}\right)^{1/3} T_9^8 \ {\rm erg\ cm^{-3}\ s^{-1}}, \tag{2}$$

where $\rho_{\rm B}$ is the baryon density, $\rho_{\rm nuc} \simeq 2.8 \times 10^{14}\ {\rm g\ cm^{-3}}$ is the nuclear saturation density, and T_9 is the temperature in units of 10^9 K. For the medium cooling processes, the PBF process, which is the latent heat released in making nucleons pair, works in accordance with the nucleon superfluid state. In terms of the type of superfluidity, neutrons in the inner crust and protons in the core become in the singlet state ($^1S_0$) and neutrons in the core become in the triplet state ($^3P_2$) if $T < T_{\rm cr}$, where $T_{\rm cr}$ is the superfluid transition temperature. The emissivity of the PBF process is approximately expressed as follows (Yakovlev & Levenfish 1995):

$$\epsilon_{\nu}^{\rm PBF} \approx 10^{21-22}\left(\frac{\rho_{\rm B}}{\rho_{\rm nuc}}\right)^{1/3} T_9^7\, \tilde{F}_i\left(\frac{T}{T_{\rm cr}}\right)\ {\rm erg\ cm^{-3}\ s^{-1}}, \tag{3}$$

where $\tilde{F}_i(T/T_{\rm cr})$ is the control function with $T/T_{\rm cr}$, which depends on the state of the nucleons ($i = s$ for $^1S_0$ and $i = t$ for $^3P_2$, Yakovlev et al. 1999):

$$\tilde{F}_s = y^2 \int_0^{\infty} dx \frac{z^4}{1+e^z}, \quad \tilde{F}_t = \frac{1}{4\pi}\int d\Omega\, y^2 \int_0^{\infty} dx \frac{z^4}{1+e^z}, \tag{4}$$

where $y = k_i T_{\rm cr}/T$, $z = \sqrt{x^2+y^2}$, and $\int d\Omega$ denotes the angle averaging procedure. k_i is a conversion factor between $T_{\rm cr}$ and the gap Δ for each state of nucleons. $\tilde{F}_i$ reaches its maximum value (unity) for $T \sim 0.5 T_{\rm cr}$ and zero for $T \lesssim 0.2 T_{\rm cr}$ (Page et al. 2004). Since the PBF process occurs through the vector or the axial channel, their coupling constants affect the emissivities. We mostly adopt values from Page et al. (2009), where the axial channel is dominant for the PBF process (Kolomeitsev & Voskresensky 2008). Generally, the PBF emissivity is higher than that of slow cooling processes in young NSs. It is noted that the crust superfluidity basically decreases the neutron specific heat, which also affects the cooling curves of young NSs (Page et al. 2009).

Depending on the kind of superfluidity/superconductivity, the typical NS age when the superfluid effect significantly contributes to their cooling curves is varied. For $^1S_0$ neutrons, the NS age where the superfluid effect can be clearly seen in cooling curves is 10–100 yr. For $^1S_0$ protons and $^3P_2$ neutrons, on the other hand, it is more than 100 yr (see Ho et al. 2015). As pointed out by Page et al. (2009, 2020), the most uncertain factor of superfluidity for NS 1987A is the strength of $^1S_0$ neutron pairing. To examine its model dependence on the cooling curves, we adopt various superfluid models of $^1S_0$ neutrons as we show in Figure 5; CCDK (Chen et al. 1993), WAP (Wambach et al. 1993), T (Takatsuka 1984), and All Paired, which assumes $T_{\rm cr} = 10^{10}$ K in $k_{F_n} < 1.48\ {\rm fm^{-1}}$. For $^3P_2$ neutron superfluidity, we adopt model "a" in Page et al. (2004) multiplied by 0.59 ($T_{\rm cr,peak} = 5.9 \times 10^8$ K, where $T_{\rm cr,peak}$ is the maximum critical temperature), which matches the recent cooling observation of the CCO detected in Cassiopeia A (see also Figure 15 in Wijngaarden et al. 2019). Compared with neutron superfluidity, the influence of proton conductivity on cooling curves under the minimal cooling scenario is much smaller (Ho et al. 2015), so we fix the model to CCDK (Chen et al. 1993).

In the photon cooling stage, the photon luminosity becomes higher than the neutrino luminosity because the temperature dependence is larger for the latter. The photon luminosity of blackbody emission can be expressed as follows:

$$L_{\gamma}(r = r_s) = 7 \times 10^{36}\ {\rm erg\ s^{-1}}\left(\frac{r_s}{10\ {\rm km}}\right)^2 T_{\rm eff,7}^4, \tag{5}$$

where $T_{\rm eff,7}$ is the effective temperature in units of 10^7 K. At ages $t \gtrsim 10^5$ yr, L_{γ} is affected by the NS surface composition. For young NSs, the surface composition significantly affects the relation between the surface and interior temperatures at $\rho \simeq 10^{10}\ {\rm g\ cm^{-3}}$ (often called the T_s–T_b relation). In order to treat the uncertainties of the surface composition, we adopt the T_s–T_b relation of Potekhin et al. (1997), who introduce the parameter:

$$\eta_{\rm PCY97} \equiv g_{s,14}^2 \frac{M_{\rm env}}{M_{\rm NS}}, \tag{6}$$

where $M_{\rm e}$ is the envelope mass and $g_{s,14}$ is the surface gravity in units of $10^{14}\ {\rm cm\ s^{-2}}$. If the NS surface is composed of heavy elements such as Fe, then $\eta_{\rm PCY97} = 0$. The upper limit of $\eta_{\rm PCY97}$ is almost exclusively determined by the strongly degenerate electron pressure, which is proportional to Equation (6) for the high-density regime due to the hydrostatic equilibrium condition (e.g., Gudmundsson et al. 1983). Since the critical pressure corresponding to the maximum value of $\eta_{\rm PCY97}$ depends on the Fermi wavenumber density of electrons (e.g., Shapiro & Teukolsky 1983), if the density gets closer to the neutron drip line, it is harder for ions to survive.

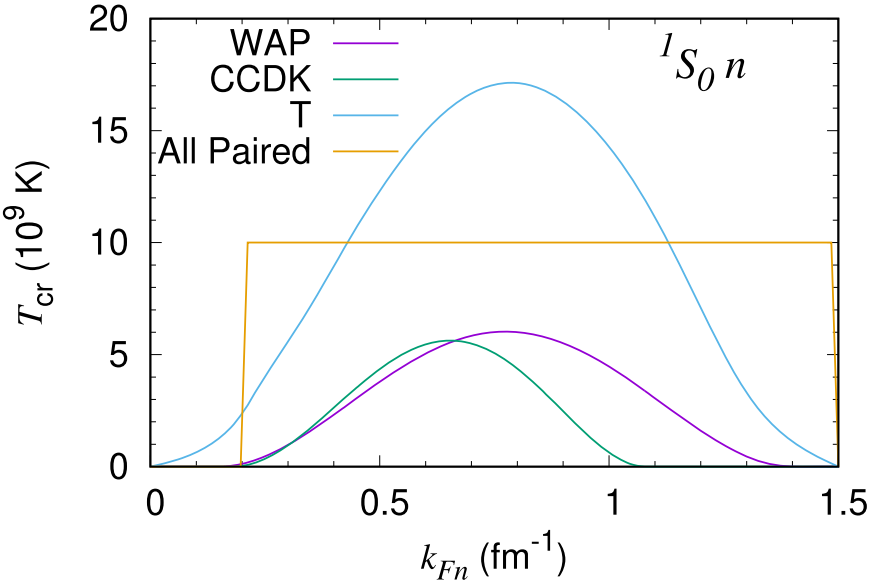

Figure 5. Adopted crust superfluid models, i.e., critical temperature as a function of Fermi wavenumber of neutrons.

From such a condition, one can get $\eta_{\rm PCY97} \lesssim 10^{-7}$ in the case that the matter is fully accreted onto the NS. The envelope model, as well as the crust superfluid model, is a crucial factor for the thermal luminosity of NS 1987A (Page et al. 2020).

In the envelope model of Potekhin et al. (1997), two cases of a pure Fe layer and a successive H-He-C-Fe layer were considered, fixing partially ionized plasma EOSs (Saumon et al. 1995; Rogers et al. 1996). In the latter case, they assumed each density of the interfaces between different elements without mixing, which could affect the T_s–T_b relation. Sophisticated envelope models have been developed to unfix their critical densities including matter mixing, but we note that their uncertainties are not so important for the T_s–T_b relation under quasi-stationary envelope evolution (Beznogov et al. 2021 and reference therein).

The temperature evolution of NSs is determined by the relativistic heat balance and heat flux equations with the NS structure, obtained by the Tolman–Oppenheimer–Volkoff (TOV) equation. For the numerical calculation of cooling curves, we use the public code `NSCool` (Page 2016) with some minor modifications (Dohi et al. 2021). The initial redshifted temperature is fixed to be 10^{10} K isothermally. Note that the cooling curves do not depend on the initial temperature for $t \gtrsim 10^{-3}$ yr (Beznogov et al. 2020).

4. Comparison between Cooling Models and Observations

First, we qualitatively compare the theoretical luminosity values with the X-ray limits[13] presented in Figure 4. In Figure 6, we show a comparison between NS cooling models and observations. As we see, the X-ray limits at $t = 31$ and 40 yr do not allow us to constrain any cooling model, even considering a higher exposure time (1 Ms) and lower confidence level (1.6σ). On the other hand, the X-ray limits at $t = 50$ yr challenge some cooling models. Therefore, we focus only on the Lynx-based upper limits in the 2040s.

The ALMA observations should also be considered to constrain the cooling models. Assuming a dust model ("ACAR" sample in Zubko et al. 1996), Cigan et al. (2019) estimated the flux density of the blob detected in SN 1987A and obtained a bolometric luminosity of (40–90)$L_\odot$ for 679 GHz flux densities of 1–2 mJy. This estimated luminosity does not directly represent the luminosity of the CCO, including uncertainties in the flux density measurements and temperature estimate. If there are additional heating effects, the luminosity of the CCO must be lower. For example, it is discussed in Page et al. (2020) that about 33% of the luminosity of the blob at 22 K may be explained by heating produced by ^{44}Ti decay.[14] Hence, it is worth mentioning that the bolometric luminosity estimated for the blob is not a direct observation of the NS and it also reflects some uncertainties derived from the dust model and the contribution of external heating, which denotes heating components by external sources apart from NSs in the thermal emission scenario ("external" heating hereafter). Moreover, if the main heating component comes from nonthermal emission, the ALMA observations can only give upper limits to the thermal luminosity and our conclusions would be significantly different from that of the thermal emission scenario. Nevertheless, we assume that the CCO is responsible for the heating of the blob as mentioned earlier, and we simply take thermal luminosities either with or without the heating corresponding to 22 K dust as the ALMA observations, whose treatment is the same as Page et al. (2020). As we see in Figure 6, the ALMA observations indicate a high thermal luminosity in the cooling theory, which implies large amounts of accreted matter onto the NS 1987A. Thus, the lower limit of

[13] We note that the luminosities present in Figure 4 are intrinsic, bolometric, and redshifted luminosities; we refer to them as "X-ray" luminosities to specify that they are derived from the X-ray data analysis in Section 2. Furthermore, we note that these luminosities are considered as upper limits in Section 2 under the assumption of nondetection of the NS in SN 1987A. However, as we will discuss later, there are cases for which we predict a possible detection of the NS by Lynx. In this latter case, the "X-ray" luminosities are "lower limits" to the NS detection. In the paper, we refer to these (upper/lower) sensitivity limits as "X-ray limits".

[14] From the observed line flux at 67.87 keV, the total mass of ^{44}Ti in the ejecta of SN 1987A was estimated as $\sim 1.5 \times 10^{-4}\ M_\odot$, where the optical depth of the ejecta for the line is evaluated as ~a few perfect (Alp et al. 2021). The estimation of the optical depth for hard X-ray/gamma-ray lines from the decay of ^{44}Ti is also about ~5% (Jerkstrand et al. 2011; Boggs et al. 2015). Thus, the assumed absorption of 33% of hard X-ray/gamma-ray lines from the decay of ^{44}Ti might be an overestimation unless other heating mechanisms work significantly.

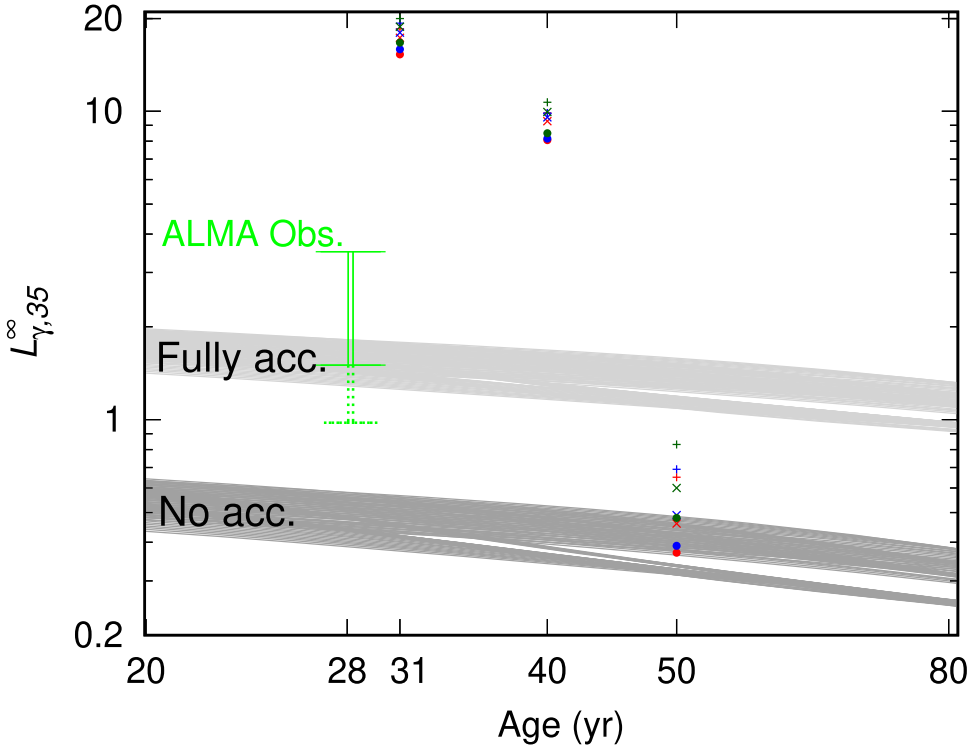

Figure 6. Comparison of the cooling curves with ALMA observational constraints of SN 1987A and X-ray limits. The ranges of the cooling model parameters in this figure are $\eta_{\rm PCY97} = 10^{-6.6}$ (fully accreted case) and $10^{-15.0}$ (no-accretion case), $M_{\rm NS} = 1.18$–$1.62\,M_{\odot}$ with a step size of $0.02\,M_{\odot}$, and five kinds of crust superfluid models: ALL Unpaired ($T_{\rm cr} = 0$), CCDK, WAP, T, and ALL ($T_{\rm cr} = 10^{10}$ K). The green error bars indicate the estimated luminosities from the ALMA observations of SN 1987A (40–90 $L_{\odot}$) with the downward extension in the case where external heating accounts for 33% of the observed blob luminosity, i.e., the lower limit from the CCO is 26 $L_{\odot}$ (Cigan et al. 2019; Page et al. 2020). Symbols denote the upper redshifted luminosities at $t = 31$, 40, and 50 yr, as in Figure 4.

the ALMA observations, including how the external heating contributed to the blob regions, is an important constraint[15].

The surface luminosity of a young NS highly depends on the NS mass, envelope mass, and crust superfluid model. In Figure 7, we show the luminosity values at $t = 31$ and 50 yr. We cover the parameter regions of $-15.0 \leqslant \log_{10}(\eta_{\rm PCY97}) \leqslant -6.6$ and $1.18 \leqslant M_{\rm NS}/M_{\odot} \leqslant 1.62$, and their parameter grid intervals are $\Delta \log_{10}(\eta_{\rm PCY97}) = 0.2$ and $\Delta M_{\rm NS} = 0.02\,M_{\odot}$, respectively. We again note that the considered mass range matches the light-curve observations of SN 1987A (Shigeyama et al. 1988; Woosley 1988; Utrobin et al. 2019; Ertl et al. 2020; Page et al. 2020).

The overall surface luminosity at $t = 31$ yr is higher than that at $t = 50$ yr by (0.2–0.4) $\times\ 10^{35}$ erg s^{-1}. If the envelope mass is higher, the luminosity is higher and this trend is valid irrespective of other parameters. If the crust superfluidity is strong, the luminosity is lower at both ages. The physical reasons derive from the enhanced cooling process of the PBF and a reduction of the neutron specific heat due to their pairing as we describe in Section 3, both of which increase the cooling rate of the NS. The trend of crust superfluidity can be clearly seen in the $M_{\rm NS}$–$\eta_{\rm PCY\,97}$ plane: if the crust superfluidity becomes stronger, the regions with $L^{\infty}_{\gamma,35} < 0.5$ (light purple) for $t = 31$ yr and $L^{\infty}_{\gamma,35} < 0.4$ (dark purple) for $t = 50$ yr become wider, extending toward higher-mass regions.

The X-ray limits in 2027 (2037) are valid only if Chandra (Lynx) will not detect thermal X-rays of NS 1987A before 2027 (2040s). It is also noted that Lynx will not be launched until the 2040s (see Section 4.3). Then, if the luminosity of NS 1987A is higher than the X-ray limits at that time, NS 1987A should be detected. As we see in Figure 8, the sensitivity limits for a 1 Ms Lynx spectrum challenge some theoretical cooling models, which should take the luminosity values between the nonaccreted matter ($\eta_{\rm PCY97} = 10^{-15}$) and fully accreted matter ($\eta_{\rm PCY97} = 10^{-6.6}$) cases. Thus, we can consider two possible scenarios, that is, the nondetection scenario and the detection scenario of the CCO by Lynx. Considering that Lynx is going to be launched in 2036 (The Lynx Team 2018; see Section G-3 and Table G-3 in this paper), since the sensitivity of Chandra is not good compared with Lynx, as we see in Figure 6,[16] the CCO in SN 1987A is unlikely to be detected until 2036.[17] Hence, discussing both the detection and nondetection of the CCO by Lynx seems worthwhile. We discuss the two scenarios also taking into account the constraints of the ALMA observations in Sections 4.1 and 4.2, respectively.

4.1. Nondetection Case of NS 1987A

If the thermal emission from NS 1987A will not be detected by Lynx, the NS cooling models could be constrained by the Lynx X-ray limits. In Figure 8, we compare the cooling models with the ALMA observations and the Lynx upper limits. We choose three envelope models

[15] We assume that the main heating component is thermal emission emitted at the NS surface. Hence, the external heating considered here does not include synchrotron heating from the PWN (Greco et al. 2021, 2022); this is completely another scenario.

[16] The reason for the difference of the sensitivity steams from the effective area: at $T = 1$ keV, it is 2 m^2 for the X-ray telescope of Lynx while it is 0.08 m^2 for Chandra. The on-axis angular resolution is almost the same, $\sim$0.5 arcsec.

[17] There are other X-ray satellites which will be launched in the near future, but they all have lower spatial resolution than Chandra, such as XRISM ($\sim 1\farcs2$) and Athena ($\sim 5''$).

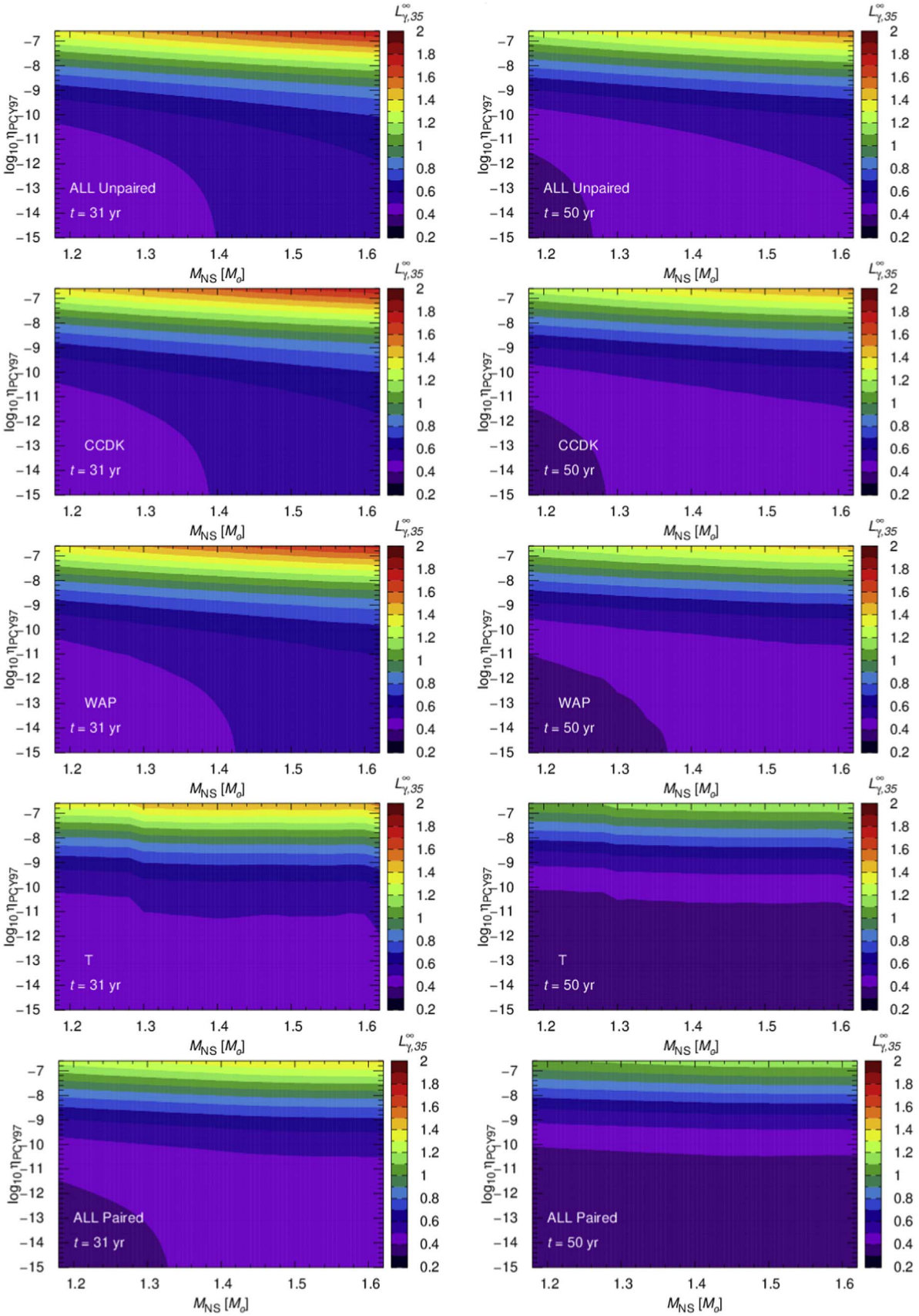

Figure 7. The values of the redshifted bolometric luminosity $L^{\infty}_{\gamma,35}$ (in units of 10^{35} erg s^{-1}) in the M_{NS}–η_{PCY97} plane. The age of the NS is $t = 31$ yr in the left panels while it is $t = 50$ yr for the right panels. From the top to bottom panels, the crust superfluid models are All Unpaired, CCDK, WAP, T, and All Paired, respectively.

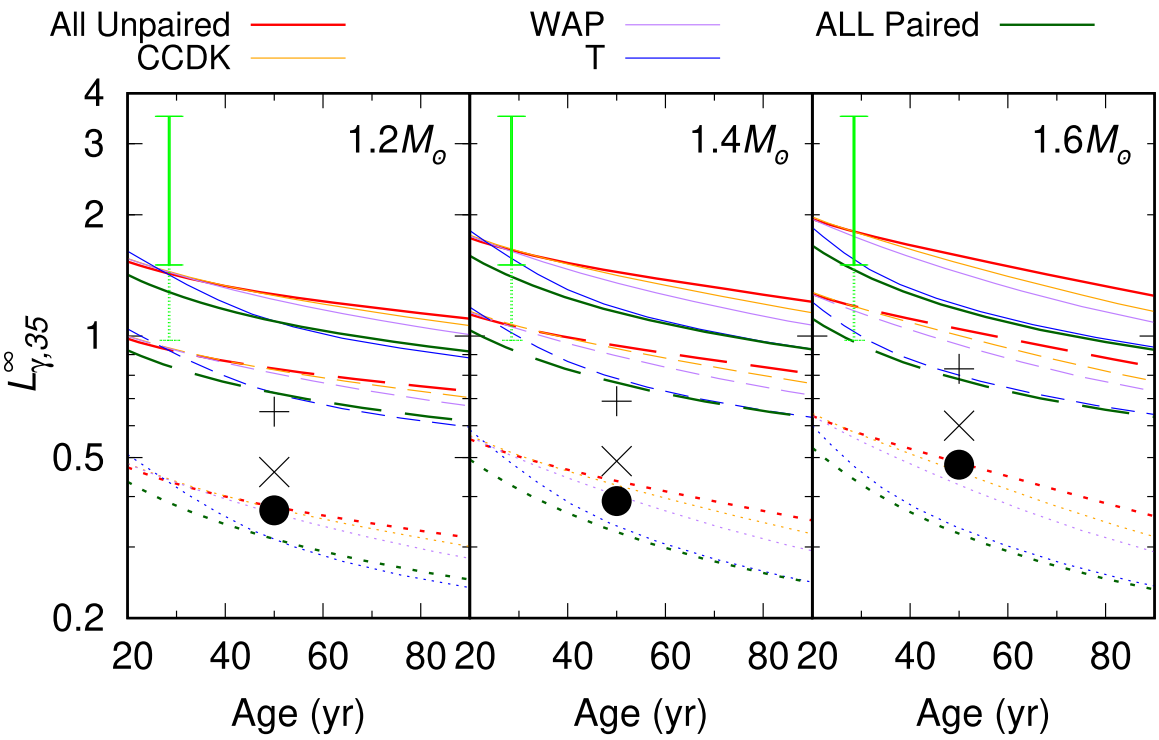

Figure 8. Same cooling curves as Figure 6 but limited to 1.2, 1.4, and 1.6 $M_{\odot}$ stars. $\eta_{\rm PCY} = 10^{-6.6}$ for the solid curves, $\eta_{\rm PCY} = 10^{-8}$ for the dashed curves, and $\eta_{\rm PCY} = 10^{-15}$ for the dotted curves. As shown in Figure 6, the circle, cross, and plus symbols indicate the bolometric upper limits in the 2040s, as discussed in Section 2, assuming a kick velocity of 300 km s^{-1}, 500 km s^{-1}, and 700 km s^{-1}, respectively.

of $\eta_{\rm PCY97} = 10^{-6.6}$, 10^{-8}, 10^{-15} and NS masses of $M_{\rm NS} = 1.2$, 1.4, 1.6 $M_{\odot}$, respectively. NS cooling models with the highest envelope mass of $\eta_{\rm PCY97} = 10^{-6.6}$ are always compatible with the ALMA observation. Meanwhile, the Lynx upper limits prefer the lower envelope models of $\eta_{\rm PCY97} \sim 10^{-15}$, whose luminosity is almost the same with the nonaccreted matter models. Thus, the two extreme models for the envelope mass cannot be compatible with both observations simultaneously, although if the contribution for external heating in the ALMA observations is even higher, the cooling curves might be consistent with the ALMA observations even considering a low-mass envelope. In the fine-tuned moderate envelope masses, both observations could be explained by choosing strong crust superfluid models. This is because the observational luminosity inferred by ALMA at 28 yr is high while the Lynx upper limits are low compared with ALMA, which implies that rapid cooling triggered by crust superfluidity around $t \sim 40$ yr is required. For example, the 1.6 $M_{\odot}$ star model with $\eta_{\rm PCY97} \lesssim 10^{-8}$ and the crust superfluid model of T can account for the ALMA observations and the Lynx upper limits with $v_{\rm kick} = 700$ km s^{-1}. Thus we find that the two following requirements must be satisfied at the same time to account for the independent observations:[18]

1. Accreted matter must exist on NS 1987A, but the envelope mass is severely constrained.
2. Rapid cooling must have occurred around $t \simeq 40$ yr.

The first remark implies that most cooling models would be rejected with a nondetection, except $\eta_{\rm PCY} \simeq 10^{-8}$ for the APR EOS. The second remark implies that the PBF process powerfully works in the crust, and thus, crust superfluidity must be vital in the adjusted $\eta_{\rm PCY97}$ values. This means that the future X-ray observations by Lynx are rather important to test NS cooling models. On the other hand, for $M_{\rm NS} = 1.2$, 1.4 $M_{\odot}$ stars, there are no parameter regions able to explain both observations. There are two reasons for this. One is that the Lynx upper limits are higher with a higher mass due to the higher redshift of blackbody radiation, as mentioned in Section 2. The other one is the difference between $g_{s,14}$ values, which slightly change the initial relaxation timescale (see Figure 9 and compare between Models A and C in Beznogov et al. 2020). According to that, the theoretical luminosity with $t = 10^{0-2}$ yr tends to be higher for higher $g_{s,14}$ values. Although the EOS uncertainties (including the heat capacity and the conductive opacity) may change the consistency, the NS mass could also be constrained depending on the envelope and crust superfluid models.

Using various cooling models, we investigate the allowed parameter regions for the ALMA lower limits and the Lynx upper limits by comparing the theoretical luminosity with the observational one in each grid. First, we show the ALMA observational constraints on the cooling models of NS 1987A in Figure 9.

As reported by Page et al. (2020), the ALMA observations reject many cooling models except high-mass envelopes, and weaker crust superfluidity is preferred in some envelope masses. For higher NS masses, the allowed regions become wider because the theoretical luminosity value is higher for higher mass. These trends are valid regardless of how the external

[18] If the external heating to the observed blob is more significant than considered here (33%), lower v_{kick} and envelope mass values can be allowed. However, although we assume the thermal emission scenario, the external heating, as representative of ^{44}Ti, may not work as effectively as described in footnote 4, meaning the ALMA observations may provide, at least, lower limits on the luminosity; therefore, the qualitative constraints are expected to be unchanged.

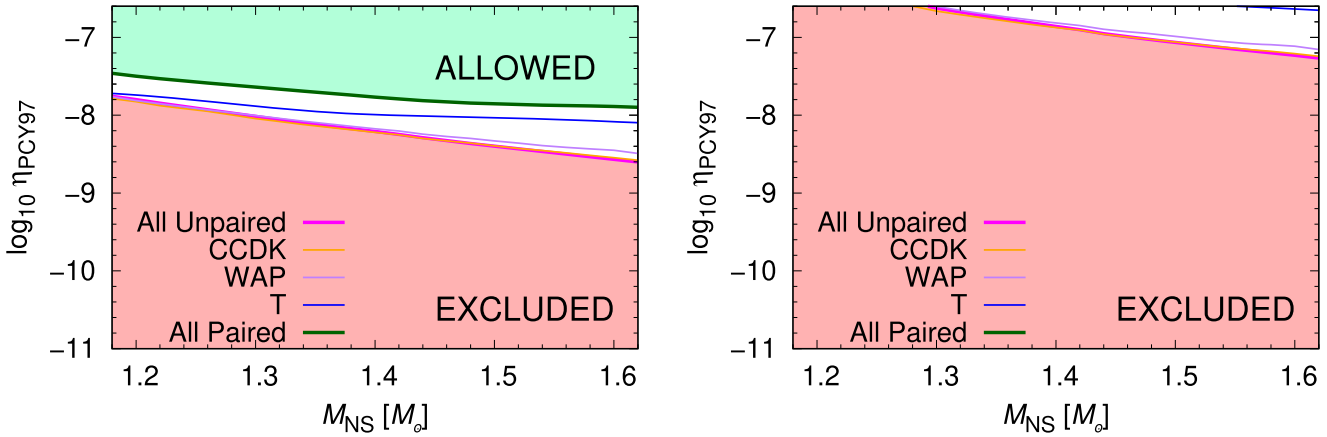

Figure 9. Constraints on cooling models (i.e., NS mass, envelope mass, and crust superfluidity) of NS 1987A from the ALMA observations, where the lower luminosity value is 26 $L_\odot$ (left) and 40 $L_\odot$ (right), corresponding to the percentage of the external heating in the observed blob being 33% and 0%, respectively. Whether noncolored regions are allowed or excluded depends on the adopted crust superfluid model.

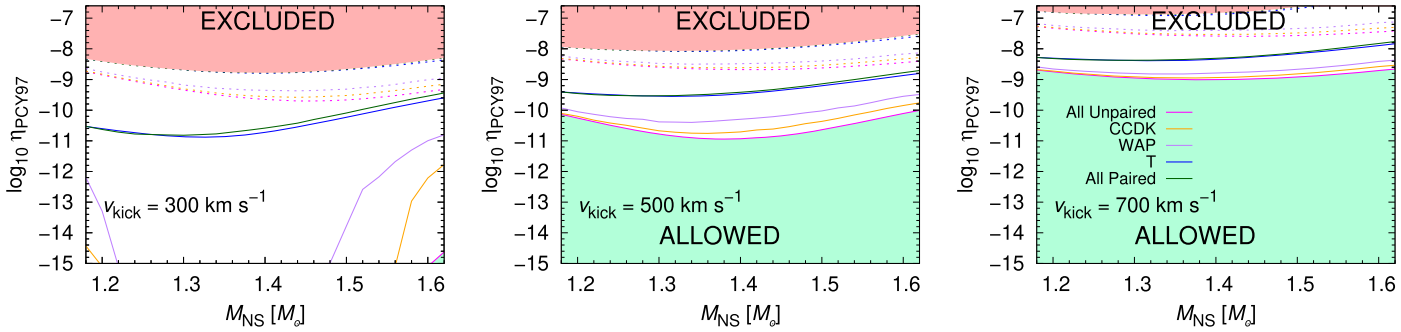

Figure 10. Constraints on cooling models from the Lynx spectra with an exposure time of 1 Ms (2σ errors for solid curves, 3σ for dotted). Three cases of the NS kick velocities, $v_{\rm kick} = 300$ km s^{-1} (left), 500 km s^{-1} (middle), and 700 km s^{-1} (right), are shown. Excluded regions are shown in red color, allowed in green. The noncolored area reflects the uncertainty in the superfluidity model, and might be allowed or excluded depending on the assumed one.

heating, except thermal emission, contributes to the observed blob luminosity. If the external heating does not contribute to the observed blob in SN 1987A, the NS mass could be automatically constrained for some crust superfluid models because of $\eta_{\rm PCY97} \lesssim 10^{-7}$; for example, we can give $M_{\rm NS} > 1.4\,M_\odot$ for the strong crust superfluid model of All Paired.

Second, we show the constraints of the Lynx upper limits in Figure 10. For the Lynx upper limits except for $M_{\rm NS} = 1.2$, 1.4, and 1.6 $M_\odot$, we take a quadratic interpolation among them. The most crucial parameter providing constraints on the cooling models is the NS kick velocity, $v_{\rm kick}$. As mentioned in Section 2, the X-ray limits of higher $v_{\rm kick}$ values become higher, which allow more cooling models. This can be clearly seen in Figure 10: for $v_{\rm kick} = 300$ km s^{-1} with 2σ errors, the NS mass could be constrained with weak crust superfluid models. To satisfy both constraints by ALMA and Lynx, the most important parameter for the cooling models is the envelope mass, which must be small. The second one is the crust superfluidity and the third is the NS mass.

In Figure 11, we show the parameter regions constrained by the ALMA and Lynx observations. Remarkably, there is no allowed region for the case of $v_{\rm kick} = 300$ km s^{-1} because the Lynx upper limits are lower than those with other $v_{\rm kick}$. For $v_{\rm kick} = 700$ km s^{-1}, on the other hand, there are allowed regions regardless of the NS mass, considering the 3σ errors of the Lynx upper limits. We note that, if the percentage of external heating is higher than 33%, a lower $v_{\rm kick} \sim 300$ km s^{-1} is quite possible (for instance, suppose the radioactive heating to 30 K by some external sources contributes to the observed blob luminosity, then the lower thermal luminosity is reduced to 32% of the blob luminosity, $L^{\infty}_{\gamma,35} = 0.48$), which is compatible with the Lynx upper limits with $v_{\rm kick} = 300$ km s^{-1}, as we see Figure 8. For $v_{\rm kick} = 500$ km s^{-1}, only masses larger than $M_{\rm NS} \gtrsim 1.5\,M_\odot$ are allowed. Thus, our results show that the kick velocity is likely to be as high as $\sim$700 km s^{-1} for the nondetection scenario. Thus, our results show that the kick velocity is likely to be as high as 700 km s^{-1}, provided that the NS 1987A is not found by Lynx observations, i.e., the nondetection scenario. In other words, future observations of $v_{\rm kick}$ are quite important for judging the detectability by Lynx. For instance, suppose that they give low $v_{\rm kick}$ (300 km s^{-1}), then NS 1987A is likely be detected in the 2040s. Although the NS kick velocity is the most crucial parameter, other cooling model parameters could also be constrained by ALMA and Lynx. For both cases with $v_{\rm kick} = 500$ and 700 km s^{-1}, the envelope masses are likely to be higher with stronger crust superfluid models as we see in Figure 11. Thus, the crust superfluidity also affects the allowed cooling model parameters. If $v_{\rm kick} = 500$ km s^{-1}, the lower limit of the NS mass could be changed in the range from $M_{\rm NS} \simeq 1.48\,M_\odot$ to $1.56\,M_\odot$. If $v_{\rm kick} = 700$ km s^{-1}, some strong crust superfluid models with high NS mass regions, i.e., light-green (dark-green) regions, could also be allowed by the Lynx upper limits with 2σ errors and the ALMA observations with external heating (the Lynx upper limits with 3σ errors and the ALMA observations without external heating). Then, the mass of NS

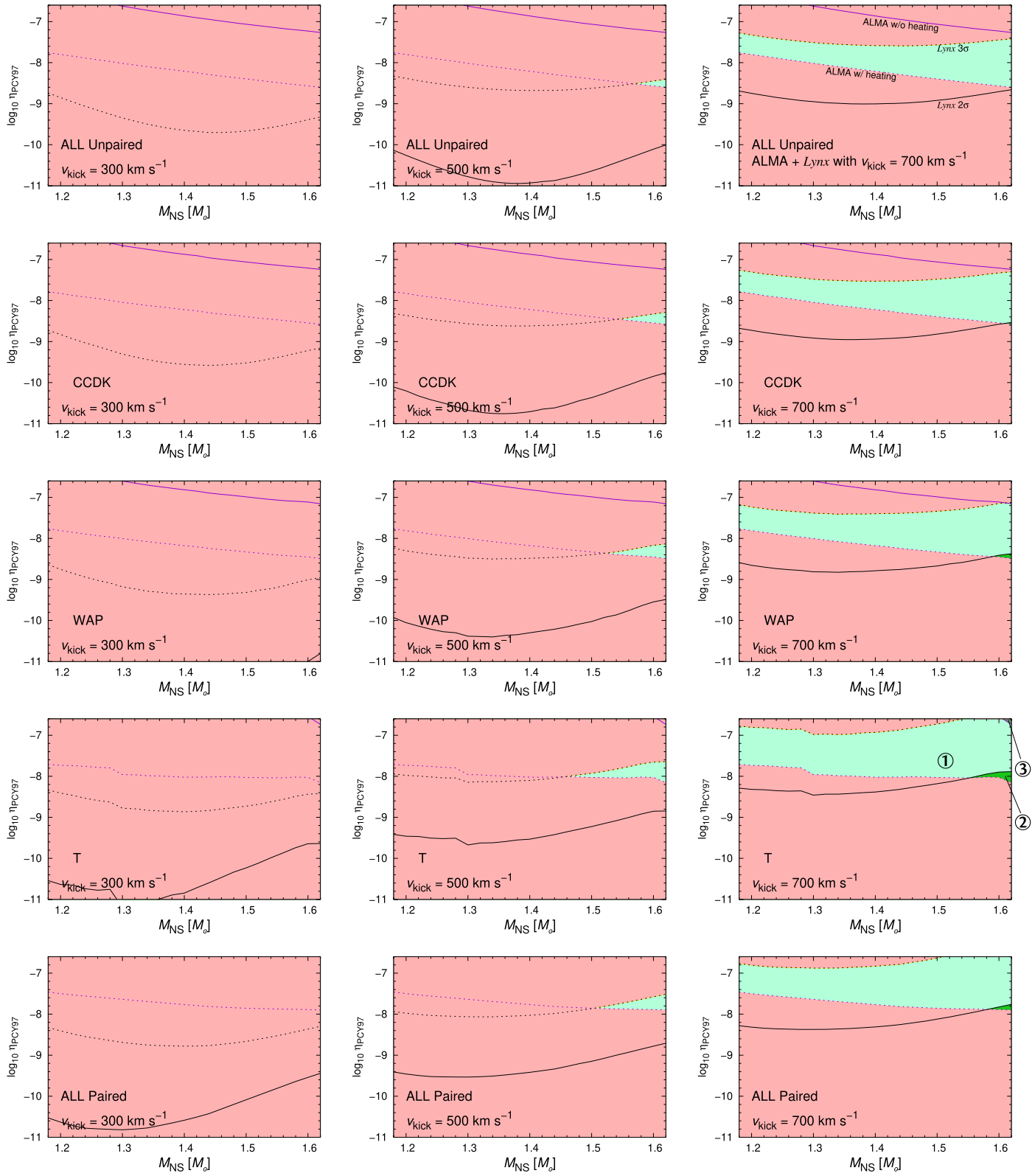

Figure 11. Constraints on NS 1987A models by the ALMA observations (purple lines: solid and dotted lines are without and with external heating, respectively) and Lynx upper limits (black lines: solid and dotted lines are for 2σ and 3σ errors, respectively) in the 2040s. Fifteen figures are shown for different v_{kick} and crust superfluid models separately. The different green colors (1–3) indicate the regions which satisfy the following observations; green (1) for the ALMA with an external heating of one-third of the blob luminosity and for the Lynx with 3σ errors, light-green (2) for ALMA with external heating and Lynx with 2σ errors, and dark-green (3) for ALMA without external heating and Lynx with 3σ errors. There are no allowed regions which satisfy both the ALMA without the external heating and the Lynx with 2σ errors.

1987A is almost determined to be $M_{NS} \sim 1.6\,M_\odot$ from the current prediction of $1.22 \leqslant M_{NS}/M_\odot \leqslant 1.62$ (Utrobin et al. 2019; Ertl et al. 2020; Page et al. 2020).

The above discussion is based on the assumption that the CCO is responsible for the heating of the blob in SN 1987A. Otherwise, i.e., in the nonthermal emission scenario, the ALMA

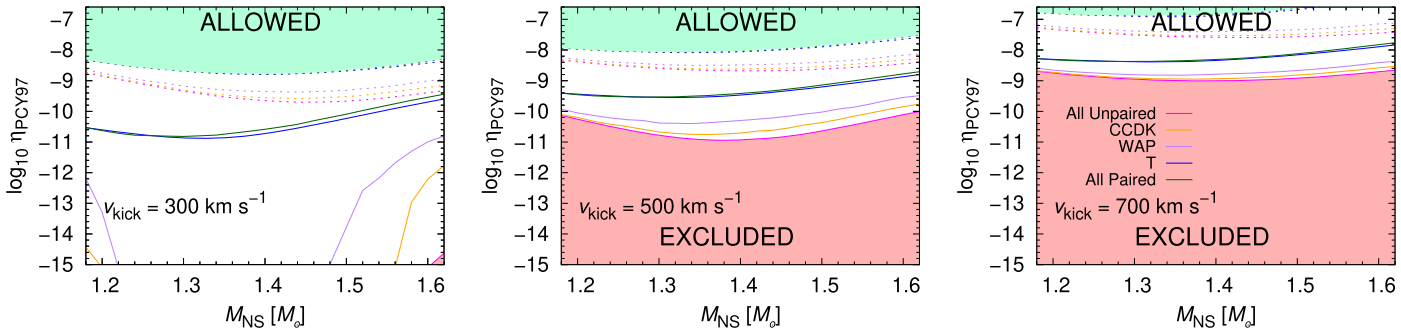

Figure 12. Same as Figure 10, but in case of the future detection of NS 1987A with Lynx.

observations can be regarded as upper limits for the thermal luminosity. Then, the allowed/excluded regions from the ALMA observational constraints in Figure 9 become opposite and most of the cooling models except with those with light envelopes could be allowed. Since both the ALMA observations and X-ray limits have upper limits in common, the Lynx X-ray limits could reject a few cooling models. In the nonthermal emission scenario, therefore, we cannot strongly mention the possibility that the CCO will be found by Lynx. Nevertheless, thermal emission from the NS is the most plausible for explaining the blob luminosity in a number of scenarios (see Table 1 in Page et al. 2020). Thus, we can conclude from Figure 11 that, if the CCO is likely not to be found by Lynx, the CCO would not contribute to the ALMA observations.

4.2. Detection Case of NS 1987A

Now suppose that blackbody radiation in SN 1987A is observed by Lynx and thus NS 1987A is confirmed to exist, i.e., the flux derived from theoretical luminosity is higher than the threshold flux obtained from that luminosity for the detection of NS 1987A with Lynx as shown in Figure 4. The parameter regions allowed for this case are shown in Figure 12. The higher the NS kick velocity is, the higher the envelope mass is. Since the Lynx data give lower luminosity limits for the detection of NS 1987A, a high envelope mass is favored, which is consistent with constraints on the envelope mass by the ALMA observations as seen in Figure 8.

Then, we also consider the ALMA constraints. The combined parameter regions of detectability are shown in Figure 13. For $v_{\rm kick} = 300\,{\rm km\,s^{-1}}$, the allowed regions are determined only by the ALMA observations. For $v_{\rm kick} = 500$ and $700\,{\rm km\,s^{-1}}$, on the other hand, some allowed regions for high NS masses could be slightly reduced compared with the original ALMA constraints, which indicates higher envelope masses. In particular, the allowed regions depend on the observational uncertainties of Lynx for *the* $v_{\rm kick} = 700\,{\rm km\,s^{-1}}$ cases. For example, if we consider the 3σ errors for the Lynx observations, a high envelope mass and high NS mass are favored.

In Figure 14, we show how the model parameters of NS 1987A can be constrained if NS 1987A that is $t \gtrsim 50$ yr old will be detected by Lynx.[19] Here, the ALMA constraints are not considered. At $t = 40$ yr (2027), the X-ray limits are derived from synthetic Chandra spectra and are around $10^{36}\,{\rm erg\,s^{-1}}$, which is higher roughly by an order of magnitude than that expected for thermal emission from the NS in the 2040s. Therefore, there is little chance to identify the CCO by detecting thermal X-ray emission directly in 2027.

On the other hand, the upper limits of Lynx are comparable to the theoretically calculated thermal luminosities, so there is some chance to detect the CCO. Depending on the observed redshifted luminosity L_γ^∞ at $t \gtrsim 50$ yr, the NS kick velocity could be constrained. Let us assume $M_{\rm NS} = 1.6\,M_\odot$ and $L_\gamma^\infty(t = 50\,{\rm yr}) = 5 \times 10^{34}\,{\rm erg\,s^{-1}}$, then the NS kick velocity can be speculated as $v_{\rm kick} < 500\,{\rm km\,s^{-1}}$, which is consistent with $v_{\rm kick} \lesssim 700\,{\rm km\,s^{-1}}$ from the ALMA observations. Thus, we can conclude that the NS in SN 1987A could be detected by Lynx around 2040 as long as the thermal emission scenario is correct.

4.3. On the Delay of Lynx Being Launched

We discussed the scenario of the NS 1987A being detected in the 2040s, but in reality, took both theoretical and X-ray luminosities in 2037, due to the limitation of the ejecta profile made up to 2037 (Orlando et al. 2020). While 2037 was the desired launched year according to the Lynx interim report (The Lynx Team 2018), the recent subsequent NAS Decadal Survey did not recommend the development of Lynx on such an early timescale (National Academies of Sciences, Engineering, & Medicine 2021): the early 2040s seems realistic as the launch year as a result of reasonable assessments of the budget profile, scientific performance, and technology risk.[20] Considering the delay in the launch of Lynx, we assume 2043 as the launch year, and estimate the X-ray limits at that time in the same manner as the spectral fitting in 2037. In our absorption model of `TBabs*(vnei +vnei+vphabs(zashift(bbodyrad)))`, we assume that the difference in the spectral fitting between 2037 and 2043 is only due to the difference of the column density of the ejecta.[21] The variation of the column density is determined by the free expansion of the ejecta profile of SN 1987A at 2037 (Orlando et al. 2020) connected to the X-ray absorption. Since high $v_{\rm kick}$ and high-mass models tend to show higher X-ray fluxes for the detection of Lynx, we examine the most extreme scenarios of the detectability of NS 1987A, that is, ($M_{\rm NS}$, $v_{\rm kick}$) = ($1.2\,M_\odot$, $300\,{\rm km\,s^{-1}}$) and ($1.6\,M_\odot$, $700\,{\rm km\,s^{-1}}$). The

[19] Only here, we adopt $M_{\rm env}$ not $\eta_{\rm PCY97}$ because the $g_{s,14}$ value is constant for each panel for the 1.2, 1.4, and 1.6 $M_\odot$ stars, respectively. Furthermore, the envelope mass is intuitively clearer than $\eta_{\rm PCY97}$ and could be directly observed. Actually, the envelope mass is much more used in various fields related to SN 1987A than $\eta_{\rm PCY97}$, except in NS cooling theory.

[20] While the Lynx teams proposed a 15 yr program with a budget of $6.2 billion, the technical, risk, and cost evaluation analysis showed a 19 yr program with a budget of $6.9 billion. In addition to this, an additional 3+ yr are estimated to be required for all missions of Lynx according to the NAS Decadal Survey.

[21] Chemical abundances of the ejecta (along the line of sight) also affect the X-ray absorption, but over a short period of 5 yr, they are not changed at all.

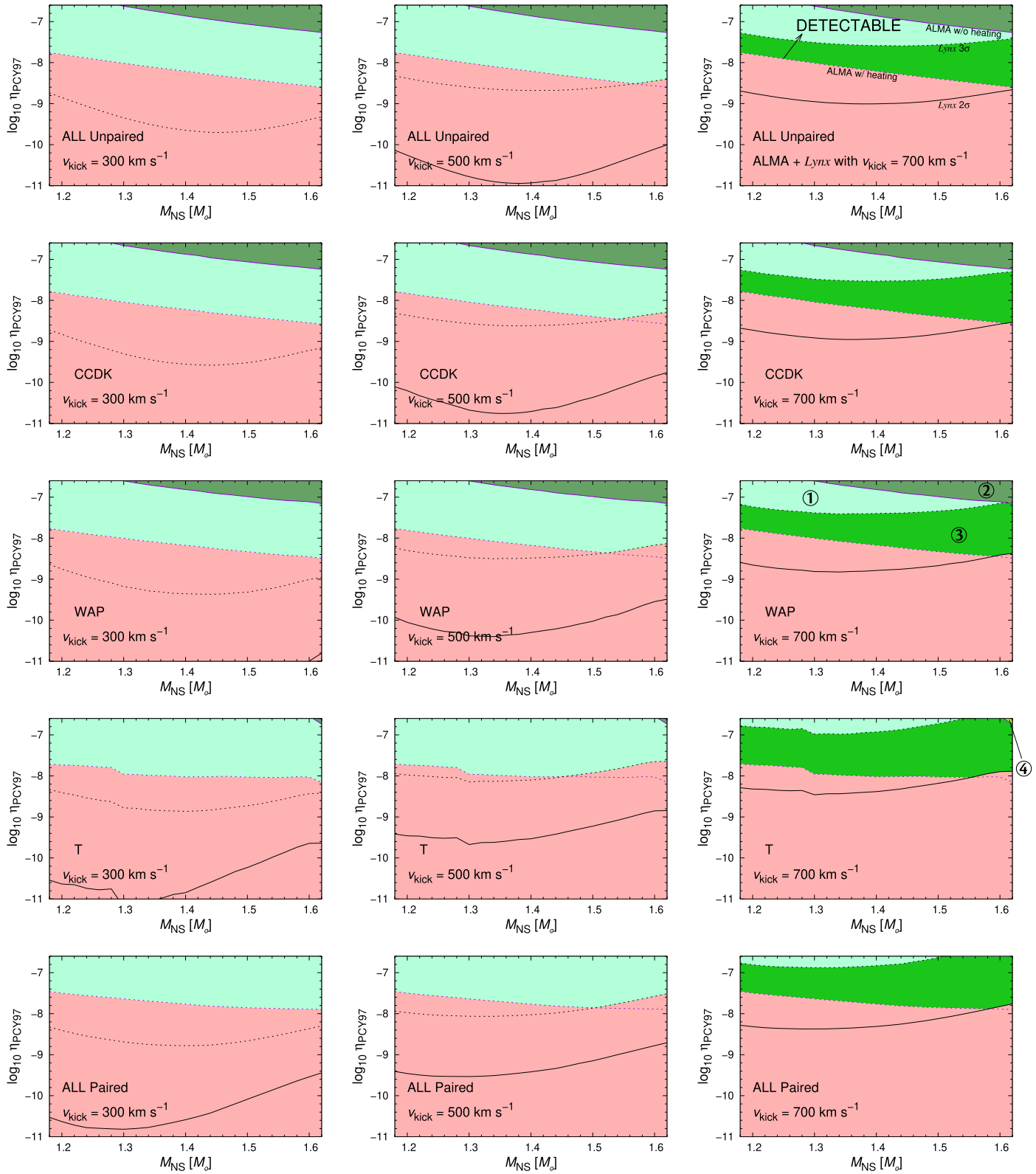

Figure 13. Constraints on NS 1987A models by ALMA observations and Lynx lower limits for a possible detection of NS 1987A that is $t \gtrsim 50$ yr old. The lines, adopted models, and observations including their uncertainties (color) for each panel are the same as Figure 11, but we add the pea-green (4) regions of the observationally possible detection satisfying the ALMA observations without external heating and Lynx observations with 2σ errors.

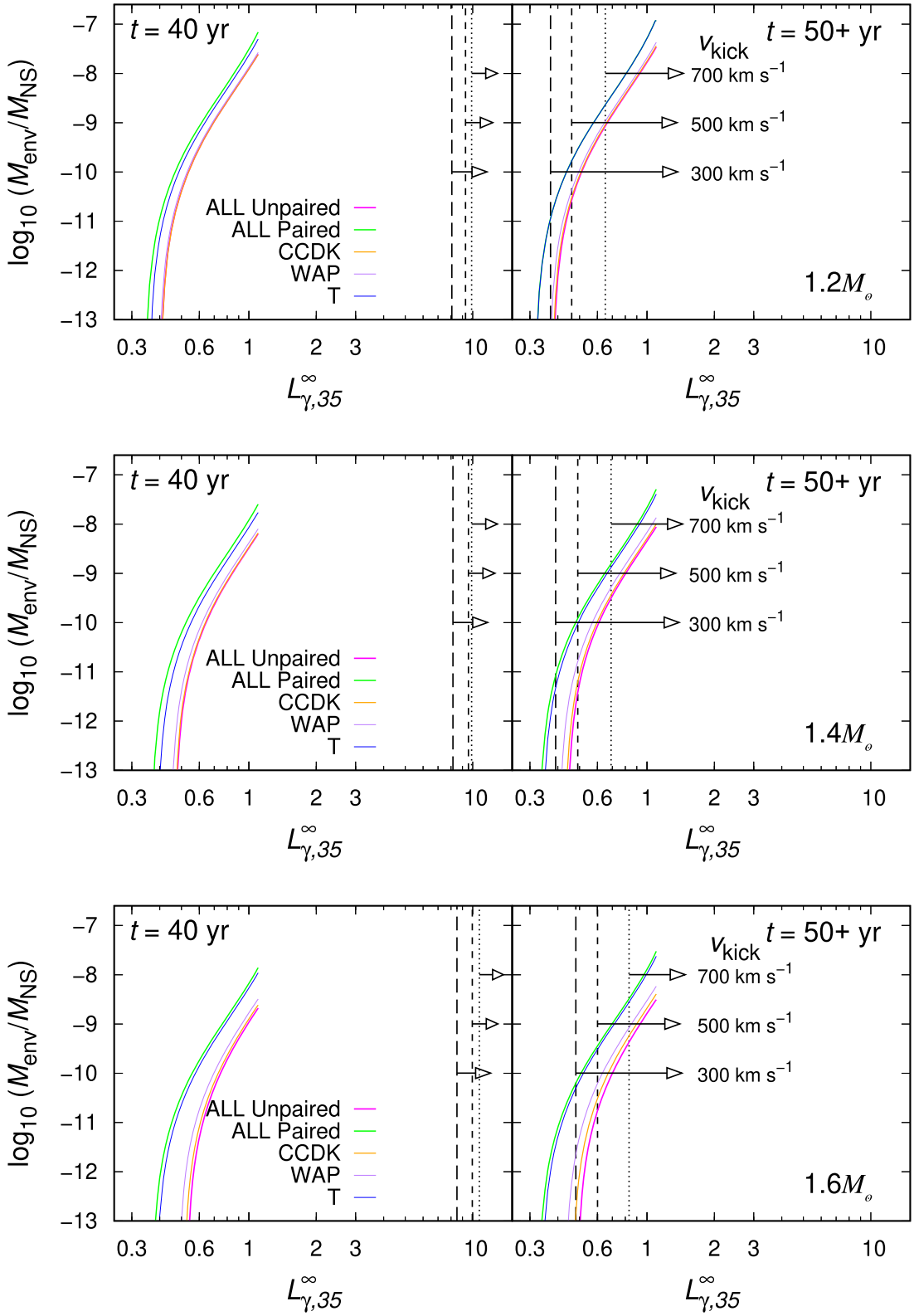

Figure 14. Cooling models (solid lines) in the plane of the envelope mass and the redshifted luminosity. The lower redshifted luminosity limits for the detection of NS 1987A by Chandra (left: $t = 40$ yr) and Lynx (right: $t = 50$ yr) are also shown for the NS kick velocities of 300 km s^{-1} (long dashed line), 500 km s^{-1} (dashed line), and 700 km s^{-1} (dotted line) with 2σ errors. From top to bottom panels, the NS masses are $1.2M_{\odot}$, $1.4M_{\odot}$, and $1.6M_{\odot}$, respectively.

Table 3
Some X-Ray Luminosity Limits for the Detectability of NS 1987A with a 1 Ms Exposure Time

($M_{\rm NS}$, $v_{\rm kick}$)	Confidence Level	X-ray limit in 2037 (10^{35} erg s^{-1})	X-ray limit in 2043 (10^{35} erg s^{-1})
(1.2 $M_\odot$, 300 km s^{-1})	99.7%	0.56	0.41
	90%	0.37	0.28
(1.6 $M_\odot$, 700 km s^{-1})	99.7%	1.25	0.81
	90%	0.83	0.55

results are shown in Table 3. As we can see, the decrease of the X-ray limit for the former scenario is roughly 25%, while for the latter scenario is 35%.[22]

In our minimal NS cooling models, the decrease in the theoretical luminosity between 2037 and 2043 results in 2%–7% depending on crust superfluidity, mass, and $\eta_{\rm PCY\ 97}$. Such mild NS cooling is due to its youth, which implies that the thermal relaxation time has not been reached yet without fast cooling processes. Thus, the net decrease of the critical luminosity for the detection of NS 1987A between 2037 and 2043 can be estimated to be ∼20%–30%, which leads to a little higher possibility to detect NS 1987A by Lynx with the passage of years compared to that deduced in this work. Nevertheless, since such a variation does not change the model constraints in 2037 significantly, we can conclude that our results presented so far qualitatively hold not only in 2037 but also 2043. Namely, it does not matter that there may be some delay in obtaining Lynx observations for our study. Thus, we again suggest that Lynx is the most promising X-ray satellite for the detection of NS 1987A regardless of the possible delay.

5. Discussion and Concluding Remarks

In this paper, we investigated the thermal emission scenario for the hot dust blob in SN 1987A, focusing on the consistency of cooling models with the ALMA and Chandra observations and the possible future detection of the CCO by Chandra and Lynx X-ray observations. We derived the following main conclusions:

1. In all cooling models presented in this paper, the luminosities are lower by orders of magnitudes than the upper limits derived from Chandra data, which therefore cannot constrain any model parameters. Hence, according to our results, currently it is almost impossible for Chandra to detect the CCO.
2. The theoretical luminosities are comparable with the upper limits derived for Lynx in the 2040s. Namely, several cooling models with high-mass envelopes can be excluded if the CCO will not be detected before the 2040s. The higher the NS kick velocity, the higher the upper limit, and more cooling model parameters are allowed.
3. The constraints on the model parameters by the Lynx upper limits, i.e., the nondetection case, are in contrast with the ALMA observational constraints, although this contrast might disappear considering higher percentages of external heating. Hence, most NS cooling models could potentially be rejected by combining the two independent observations. As a result of the detailed constraints, the NS kick velocity is likely to be as high as ∼700 km s^{-1}, assuming that the CCO is responsible for the heating of the blob. For X-ray observations of the high kick velocity, the NS mass is preferred to be as high as ∼1.6 $M_\odot$. According to models that satisfy the constraints from both observations, the envelope mass must be as high as $\sim 10^{-8} M_{\rm NS}$. At the same time, a rapid neutrino cooling process, which is likely to be PBF triggered by crust superfluidity, must work at $t \simeq 40$ yr.
4. Since the Lynx upper limits (at $t = 50$ yr) are comparable to the theoretical luminosities, Lynx could succeed in detecting the NS 1987A that is 50+ yr old. The NS must have a high envelope mass in most cases, especially for $v_{\rm kick} = 700$ km s^{-1}. Thus, launching the Lynx satellite as early as possible is desired for the detection of the youngest NS.
5. Even with some delay of Lynx being launched up to the early 2040s, our results are not so changed compared to those in 2037.

In the present study, the assumed kick velocity of NS 1987A is one of key parameters for constraining other NS properties through the estimation of the X-ray absorption and the upper (lower) intrinsic luminosities in case of nondetection (detection). Theoretically, it has been expected that newly born NSs are kicked by an asymmetric explosion, aided by the so-called gravitational tugboat mechanism (Wongwathanarat et al. 2013; Janka 2017) and/or by anisotropic neutrino emission (e.g., Woosley 1987; Socrates et al. 2005). The recently found lepton number emission self-sustained asymmetry (LESA; Tamborra et al. 2014) could also contribute to the acceleration of NSs, although the contribution may not be so large (Bollig et al. 2021). Meanwhile, observed NS kick velocities for young pulsars typically range over several 100 km s^{-1} (e.g., Faucher-Giguère & Kaspi 2006) with some exceptions of over 1000 km s^{-1} (Chatterjee et al. 2005). Additionally, analyses of X-ray observations of several SNRs (Katsuda et al. 2018) have supported a hydrodynamical origin of NS kicks related to anisotropic mass ejection (Burrows & Hayes 1996; Nagataki 2000; Wongwathanarat et al. 2013). The explosion of SN 1987A has been suggested to have been asymmetric from observed line emission, e.g., iron lines ([Fe II]; Haas et al. 1990) and gamma-ray lines from the decay of ^{44}Ti (Schwarz et al. 2011). Actually, the 3D morphology of the inner ejecta of SN 1987A is globally asymmetric with an elongated structure (e.g., Larsson et al. 2013, 2016), which was foreseen in some early numerical simulations of SN 1987A (Nagataki et al. 1997, 1998; Nagataki 2000). Thus, a kick to NS 1987A has highly been expected from such observations. In the 3D MHD model (Orlando et al. 2020) used for the estimation of the X-ray limits, the NS kick velocity of NS 1987A was estimated as approximately 300 km s^{-1} by assuming momentum

[22] Note that these variations are quite similar to the reduction of the ejecta density assuming free expansion, 28.8%. Thus, the time evolution of the sparseness of shocked ejecta roughly corresponds to that of the decrease of X-ray limits.

conservation. Therefore, the range of NS kick velocity values considered in this work (300–700 $\mathrm{km\,s^{-1}}$), which represent both the detection and nondetection scenarios, is roughly consistent with the observed values for young pulsars as well as that suggested from the ALMA observations (Cigan et al. 2019). In the 3D model, the explosion was, however, artificially initiated with an ad hoc asymmetry (asymmetric thermal bomb; Ono et al. 2020), and the early evolution (<1 s) of the shock revival including fall back was not treated in a realistic way. Although the 3D model (Ono et al. 2020; Orlando et al. 2020) explains both the observed asymmetric line profiles of iron (Haas et al. 1990) and titanium (Boggs et al. 2015) and the X-ray light curves (e.g., Frank et al. 2016) well with a blue supergiant progenitor model resulting from a binary merger (Urushibata et al. 2018), the estimated value may only provide a reference value. Hitherto, recent 2D and 3D more self-consistent neutrino-driven core-collapse SN simulations (e.g., Nagakura et al. 2017, 2019; Bollig et al. 2021; for SN 1987A; Nakamura et al. 2022) have tried to figure out NS properties. A consensus on the magnitudes of NS kick velocities has, however, not been achieved yet. Therefore, future determination of the kick velocity of NS 1987A based on the detection by Lynx will shed light not only on the NS properties but also on the explosion mechanism and the origin of the explosion asymmetries.

We fix the NS EOS as the APR model in this paper. However, the NS EOS in high-density regions, including the internal composition, has significant uncertainties even with recent experiments and observations (for a review, see Burgio et al. 2021). A crucial problem for NS cooling theories is the presence or absence of the DU process in the core. Since we limit the NS mass as $1.2 \leqslant M_{\rm NS}/M_{\odot} \leqslant 1.6$ according to recent predictions (Utrobin et al. 2019; Ertl et al. 2020; Page et al. 2020), we do not consider the possibility that the DU process occurs for the APR EOS. However, in the case of large symmetry energy EOSs, theoretical luminosities should be decreased due to effective neutrino cooling by the DU process, which could change the consistency with the observations of SN 1987A. Although the recent experiment to measure the neutron skin thickness of ^{208}Pb, the updated lead Radius EXperiment (PREX-2), resulted in a symmetry energy value of the slope parameter of $L = (106 \pm 37)$ MeV (Reed et al. 2021; but see also Reinhard et al. 2022), most experiments and observations show a relatively low symmetry energy of $L \simeq 60 \pm 20$ MeV (e.g., Sotani et al. 2022). Since the L value has a negative correlation with the threshold mass of the DU process (Dohi et al. 2019), the DU process is likely not operating in NS 1987A because of the inferred low-mass NSs.[23]

Beyond the nucleon DU process, other rapid cooling processes through exotic states such as hyperon DU processes and deconfined quark beta decay may also work and cool young NSs rapidly. However, a concern for the rapid cooling scenario for NS 1987A is that the young NS probably has a nonisothermal temperature structure where the crust is hotter than the core. In other words, unless there are large regions where the rapid cooling processes work (in relatively lower-density regions), only the heat in the crust, not in the core, may be transported to the surface, so that the rapid cooling processes may not affect the luminosity around the age of NS 1987A. A candidate as an effective exotic cooling process which appears in lower-density regions is the pion condensation process, although it can significantly soften the EOS enough not to support 2 $M_{\odot}$ stars (Dohi et al. 2022). In that sense, the minimal cooling scenario considered here seems reasonable for NS 1987A.

For young NSs around at $t \sim 10$ yr, the most crucial cooling process is the PBF process triggered by crust superfluidity (Page et al. 2009) because of the nonisothermal temperature structure as described above. The efficiency of the crust PBF process is determined by the density dependence of the critical temperature, being still uncertain. Since crust superfluidity can also be probed by ultracold atom gas studies in the context of BCS–BEC crossover (for reviews, see Sedrakian & Clark 2019; Ohashi et al. 2020), investigating the detailed effects of crust superfluidity from both astrophysics and condensed matter physics is worthwhile for understanding the properties of NS 1987A.

This work also benefits from the potential high diagnostic power provided by Lynx. The significant increase in sensitivity with respect to Chandra allow us to constrain robustly some cooling models and to infer physical properties about NS 1987A and its envelope. This is true either if the putative NS 1987A is detected by Lynx or not. Future Lynx observations of SN 1987A will be crucial to shed light on the nature of this compact object.

We thank Lei Sun for giving some useful advice. We also thank the referee for careful reading and many helpful comments, which significantly improved this paper. A.D., S. N., and M.O. thank support from RIKEN Interdisciplinary Theoretical and Mathematical Sciences Program (iTHEMS) and Pioneering Program of RIKEN for Evolution of Matter in the Universe (r-EMU). This work is supported by JSPS KAKENHI grant Nos. 19H00693, JP21K03545, and 22J10448. M.M., S.O., and B.O. acknowledge financial contribution from the PRIN INAF 2019 grant "From massive stars to supernovae and supernova remnants: driving mass, energy and cosmic rays in our Galaxy". E.G. acknowledges funding from the European Union's Horizon 2020 research and innovation program under grant agreement No. 101004131 (SHARP).

Facility: Chandra.

Software: Gnuplot (Williams & Kelley 2022), CIAO (Fruscione et al. 2006), HEASOFT, XSPEC (Arnaud 1996), DS9.

Appendix
Upper Limits: Other Scenarios

In Figure 4, we showed the upper limits of X-ray luminosity at the 90% confidence level and the synthetic spectra are produced assuming an exposure time of 1 Ms. In Figures 15–17, we show the same figures with different confidence level and exposure time. Furthermore, the specific values of upper limits in all parameter sets considered in this paper are listed in Tables 4–6.

[23] One can get the empirical relation between L and the threshold mass of the DU process $M_{\rm DU}$ (Sotani & Dohi 2022) as:

$$\frac{M_{\rm DU}}{M_{\odot}} = 3.5801 - 4.2036 L_{100} + 1.5191 L_{100}^2, \quad (7)$$

where $L_{100} \equiv L/(100\,\mathrm{MeV})$. Taking the fiducial value of $L = 60$ MeV, $M_{\rm DU} \simeq 1.6048\,M_{\odot}$, which is roughly the upper mass of NS 1987A inferred from the observed SN 1987A light curves.

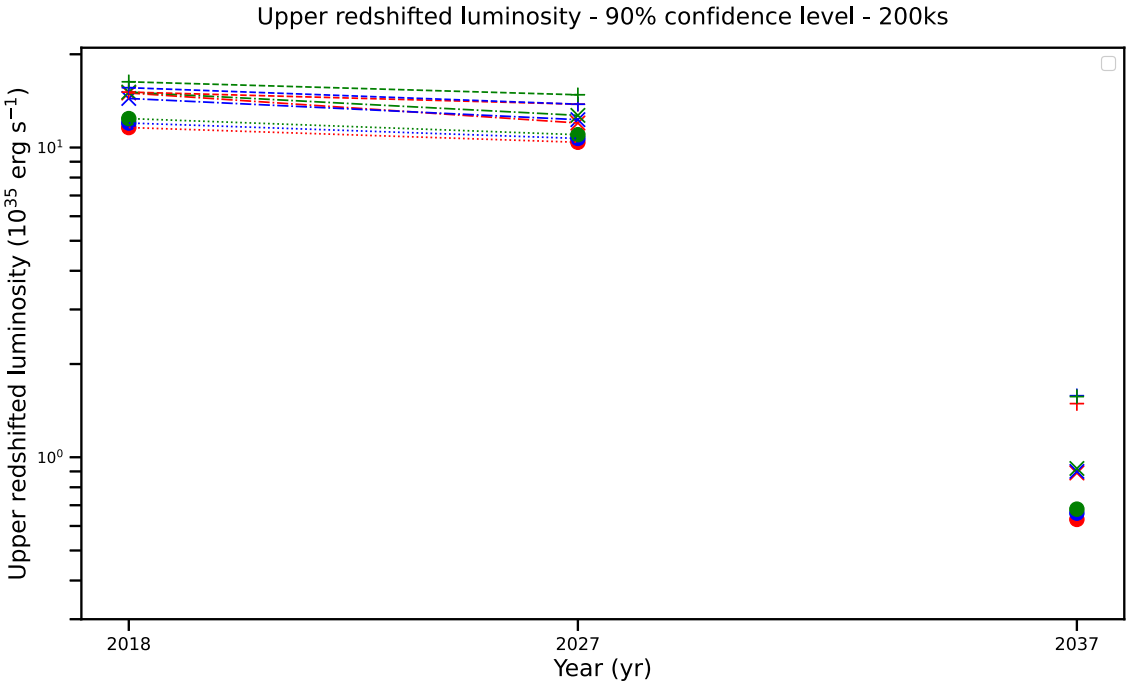

Figure 15. Same as Figure 4 but the synthetic spectra are produced assuming an exposure time of 200 ks.

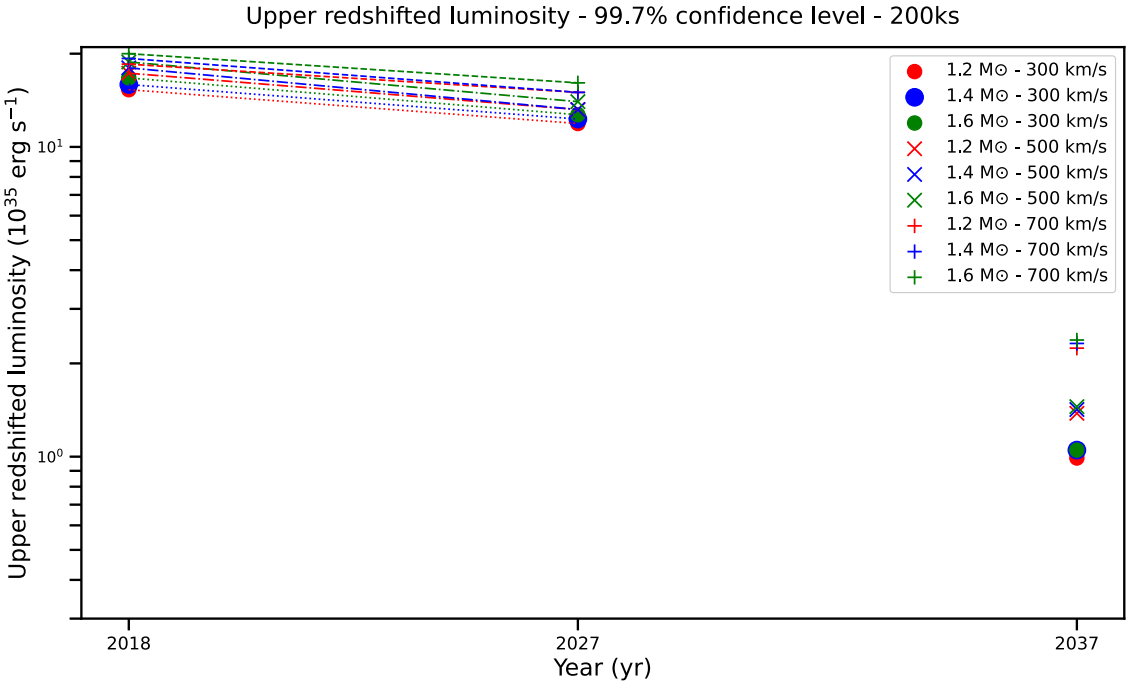

Figure 16. Same as Figure 4 but the upper limits are estimated at the 99.7% confidence level and the synthetic spectra are produced assuming an exposure time of 200 ks.

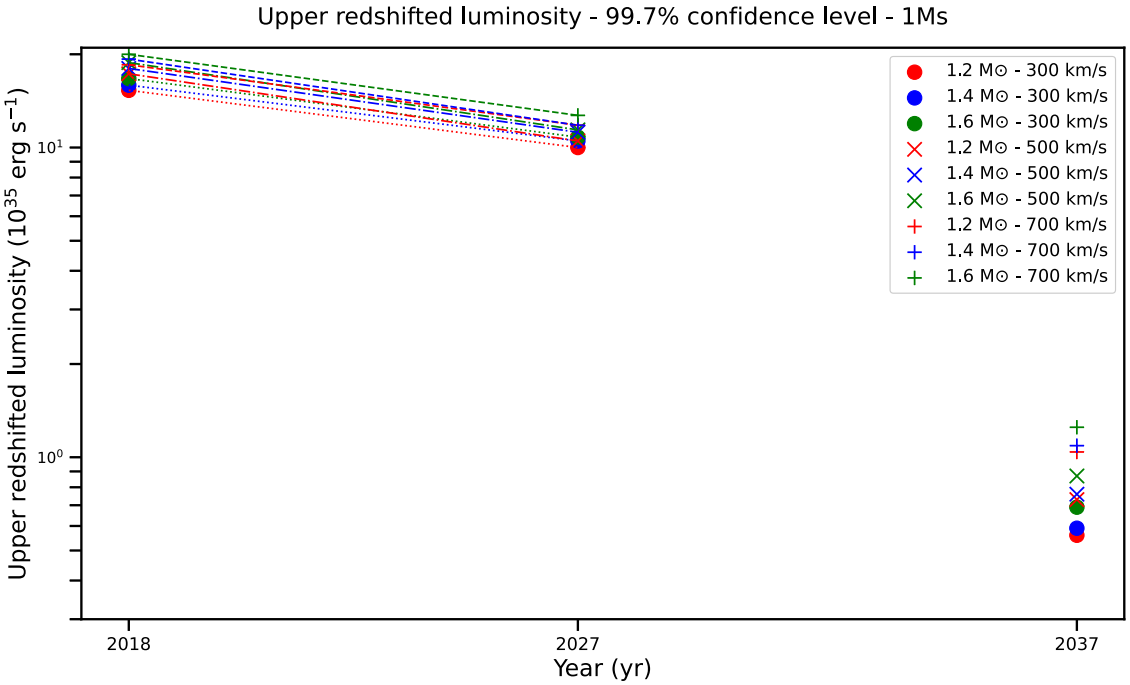

Figure 17. Same as Figure 4 but the upper limits are estimated at the 99.7% confidence level.

Table 4
Luminosity Upper Limits for a 1.2 $M_\odot$ NS

No.	Year	$v_{\rm kick}$ (km s^{-1})	Confidence Level	Exposure Time[b] (Ms)	Upper Limit[a] (10^{35} erg s^{-1})
1		700	99.7%	Table 1	18.5
2	2018	500	99.7%	Table 1	17.3
3		300	99.7%	Table 1	15.3
4		700	90%	Table 1	15.1
5	2018	500	90%	Table 1	15.0
6		300	90%	Table 1	11.6
7		700	99.7%	0.2	15.0
8	2027	500	99.7%	0.2	13.2
9		300	99.7%	0.2	11.9
10		700	90%	0.2	13.8
11	2027	500	90%	0.2	12.0
12		300	90%	0.2	10.4
13		700	99.7%	1	11.8
14	2027	500	99.7%	1	10.5
15		300	99.7%	1	10.0
16		700	90%	1	9.88
17	2027	500	90%	1	9.28
18		300	90%	1	8.06

Table 4
(Continued)

No.	Year	$v_{\rm kick}$ (km s^{-1})	Confidence Level	Exposure Time[b] (Ms)	Upper Limit[a] (10^{35} erg s^{-1})
19		700	99.7%	0.2	2.24
20	2037	500	99.7%	0.2	1.38
21		300	99.7%	0.2	0.99
22		700	90%	0.2	1.49
23	2037	500	90%	0.2	0.89
24		300	90%	0.2	0.63
25		700	99.7%	1	1.04
26	2037	500	99.7%	1	0.73
27		300	99.7%	1	0.56
28		700	90%	1	0.65
29	2037	500	90%	1	0.46
30		300	90%	1	0.37

Notes.
[a] Upper limit on the redshifted bolometric luminosity assuming a blackbody with a radius of 11.65 km and a mass of 1.2 $M_\odot$.
[b] Exposure time assumed to synthesize the 2027 Chandra and 2037 Lynx spectra.

Table 5
Luminosity Upper Limits for a 1.4 $M_\odot$ NS

No.	Year	$v_{\rm kick}$ (km s^{-1})	Confidence Level	Exposure Time[b] (Ms)	Upper Limit[a] (10^{35} erg s^{-1})
1		700	99.7%	Table 1	19.3
2	2018	500	99.7%	Table 1	18.0
3		300	99.7%	Table 1	15.9
4		700	90%	Table 1	15.6
5	2018	500	90%	Table 1	14.4
6		300	90%	Table 1	12.0
7		700	99.7%	0.2	15.0
8	2027	500	99.7%	0.2	13.2
9		300	99.7%	0.2	12.3
10		700	90%	0.2	13.8
11	2027	500	90%	0.2	12.3
12		300	90%	0.2	10.7
13		700	99.7%	1	11.8
14	2027	500	99.7%	1	11.2
15		300	99.7%	1	10.5
16		700	90%	1	9.88
17	2027	500	90%	1	9.55
18		300	90%	1	8.15
19		700	99.7%	0.2	2.32
20	2037	500	99.7%	0.2	1.42
21		300	99.7%	0.2	1.05
22		700	90%	0.2	1.58
23	2037	500	90%	0.2	0.90
24		300	90%	0.2	0.66
25		700	99.7%	1	1.09
26	2037	500	99.7%	1	0.76
27		300	99.7%	1	0.59
28		700	90%	1	0.69
29	2037	500	90%	1	0.49
30		300	90%	1	0.39

Notes.
[a] Upper limit on the redshifted bolometric luminosity assuming a blackbody with a radius of 11.57 km and a mass of 1.4 $M_\odot$.
[b] Exposure time assumed to synthesize the 2027 Chandra and 2037 Lynx spectra.

Table 6
Luminosity Upper Limits for a 1.6 $M_\odot$ NS

No.	Year	$v_{\rm kick}$ (km s^{-1})	Confidence Level	Exposure Time[b] (Ms)	Upper Limit[a] (10^{35} erg s^{-1})
1		700	99.7%	Table 1	20.0
2	2018	500	99.7%	Table 1	18.8
3		300	99.7%	Table 1	16.7
4		700	90%	Table 1	16.3
5	2018	500	90%	Table 1	15.1
6		300	90%	Table 1	12.4
7		700	99.7%	0.2	16.1
8	2027	500	99.7%	0.2	14.0
9		300	99.7%	0.2	12.7
10		700	90%	0.2	14.8
11	2027	500	90%	0.2	12.7
12		300	90%	0.2	11.0
13		700	99.7%	1	12.7
14	2027	500	99.7%	1	11.4
15		300	99.7%	1	10.8
16		700	90%	1	10.7
17	2027	500	90%	1	9.94
18		300	90%	1	8.49
19		700	99.7%	0.2	2.38
20	2037	500	99.7%	0.2	1.45
21		300	99.7%	0.2	1.05
22		700	90%	0.2	1.57
23	2037	500	90%	0.2	0.92
24		300	90%	0.2	0.68
25		700	99.7%	1	1.25
26	2037	500	99.7%	1	0.87
27		300	99.7%	1	0.69
28		700	90%	1	0.83
29	2037	500	90%	1	0.60
30		300	90%	1	0.48

Notes.
[a] Upper limit on the redshifted bolometric luminosity assuming a blackbody with a radius of 11.45 km and a mass of 1.6 $M_\odot$.
[b] Exposure time assumed to synthesize the 2027 Chandra and 2037 Lynx spectra.

ORCID iDs

Akira Dohi https://orcid.org/0000-0001-8726-5762
Emanuele Greco https://orcid.org/0000-0001-5792-0690
Shigehiro Nagataki https://orcid.org/0000-0002-7025-284X
Masaomi Ono https://orcid.org/0000-0002-0603-918X
Marco Miceli https://orcid.org/0000-0003-0876-8391
Salvatore Orlando https://orcid.org/0000-0003-2836-540X

References

Akmal, A., Pandharipande, V. R., & Ravenhall, D. G. 1998, PhRvC, 58, 1804
Alp, D., Larsson, J., & Fransson, C. 2021, ApJ, 916, 76
Alp, D., Larsson, J., Fransson, C., et al. 2018, ApJ, 864, 174
Antoniadis, J., Freire, P. C. C., Wex, N., et al. 2013, Sci, 340, 448
Arnaud, K. A. 1996, in ASP Conf. Ser. 101, Astronomical Data Analysis Software and Systems V, ed. G. H. Jacoby & J. Barnes (San Francisco, CA: ASP), 17
Beznogov, M. V., Page, D., & Ramirez-Ruiz, E. 2020, ApJ, 888, 97
Beznogov, M. V., Potekhin, A. Y., & Yakovlev, D. G. 2021, PhR, 919, 1
Bionta, R. M., Blewitt, G., Bratton, C. B., et al. 1987, PhRvL, 58, 1494
Boggs, S. E., Harrison, F. A., Miyasaka, H., et al. 2015, Sci, 348, 670
Boguta, J. 1981, PhLB, 106, 255
Bollig, R., Yadav, N., Kresse, D., et al. 2021, ApJ, 915, 28
Burgio, G. F., Schulze, H. J., Vidaña, I., & Wei, J. B. 2021, PrPNP, 120, 103879
Burrows, A., & Hayes, J. 1996, PhRvL, 76, 352
Chatterjee, S., Vlemmings, W. H. T., Brisken, W. F., et al. 2005, ApJL, 630, L61
Chen, J. M. C., Clark, J. W., Davé, R. D., & Khodel, V. V. 1993, NuPhA, 555, 59
Cigan, P., Matsuura, M., Gomez, H. L., et al. 2019, ApJ, 886, 51
Cromartie, H. T., Fonseca, E., Ransom, S. M., et al. 2020, NatAs, 4, 72
Demorest, P. B., Pennucci, T., Ransom, S. M., Roberts, M. S. E., & Hessels, J. W. T. 2010, Natur, 467, 1081
Dohi, A., Kase, R., Kimura, R., Yamamoto, K., & Hashimoto, M.-a. 2021, PTEP, 2021, 093E01
Dohi, A., Liu, H., Noda, T., & Hashimoto, M.-A. 2022, IJMPE, 31, 2250006

Dohi, A., Nakazato, K., Hashimoto, M.-a., Yasuhide, M., & Noda, T. 2019, PTEP, 2019, 113E01
Ertl, T., Woosley, S. E., Sukhbold, T., & Janka, H. T. 2020, ApJ, 890, 51
Esposito, P., Rea, N., Lazzati, D., et al. 2018, ApJ, 857, 58
Faucher-Giguère, C.-A., & Kaspi, V. M. 2006, ApJ, 643, 332
Frank, K. A., Zhekov, S. A., Park, S., et al. 2016, ApJ, 829, 40
Fruscione, A., McDowell, J. C., Allen, G. E., et al. 2006, Proc. SPIE, 6270, 62701V
Gnedin, O. Y., Yakovlev, D. G., & Potekhin, A. Y. 2001, MNRAS, 324, 725
Greco, E., Miceli, M., Orlando, S., et al. 2021, ApJL, 908, L45
Greco, E., Miceli, M., Orlando, S., et al. 2022, ApJ, 931, 132
Gudmundsson, E. H., Pethick, C. J., & Epstein, R. I. 1983, ApJ, 272, 286
Haas, M. R., Colgan, S. W. J., Erickson, E. F., et al. 1990, ApJ, 360, 257
Hirata, K., Kajita, T., Koshiba, M., et al. 1987, PhRvL, 58, 1490
Ho, W. C. G., Elshamouty, K. G., Heinke, C. O., & Potekhin, A. Y. 2015, PhRvC, 91, 015806
Hobbs, G., Lorimer, D. R., Lyne, A. G., & Kramer, M. 2005, MNRAS, 360, 974
Janka, H.-T. 2017, ApJ, 837, 84
Jerkstrand, A., Fransson, C., & Kozma, C. 2011, A&A, 530, A45
Katsuda, S., Morii, M., Janka, H.-T., et al. 2018, ApJ, 856, 18
Kolomeitsev, E. E., & Voskresensky, D. N. 2008, PhRvC, 77, 065808
Larsson, J., Fransson, C., Kjaer, K., et al. 2013, ApJ, 768, 89
Larsson, J., Fransson, C., Spyromilio, J., et al. 2016, ApJ, 833, 147
Lattimer, J. M., Pethick, C. J., Prakash, M., & Haensel, P. 1991, PhRvL, 66, 2701
Lattimer, J. M., & Prakash, M. 2016, PhR, 621, 127
Lattimer, J. M., van Riper, K. A., Prakash, M., & Prakash, M. 1994, ApJ, 425, 802
Lim, Y., Hyun, C. H., & Lee, C.-H. 2017, IJMPE, 26, 1750015
Lucy, L. B. 1974, AJ, 79, 745
Nagakura, H., Iwakami, W., Furusawa, S., et al. 2017, ApJS, 229, 42
Nagakura, H., Sumiyoshi, K., & Yamada, S. 2019, ApJ, 878, 160
Nagataki, S. 2000, ApJS, 127, 141
Nagataki, S., Hashimoto, M.-a., Sato, K., & Yamada, S. 1997, ApJ, 486, 1026
Nagataki, S., Shimizu, T. M., & Sato, K. 1998, ApJ, 495, 413
Nakamura, K., Takiwaki, T., & Kotake, K. 2022, MNRAS, 514, 3941
National Academies of Sciences, Engineering, & Medicine 2021, Pathways to Discovery in Astronomy and Astrophysics for the 2020s (Washington, DC: National Academies Press)
Ohashi, Y., Tajima, H., & van Wyk, P. 2020, PrPNP, 111, 103739
Ono, M., Nagataki, S., Ferrand, G., et al. 2020, ApJ, 888, 111
Orlando, S., Ono, M., Nagataki, S., et al. 2020, A&A, 636, A22
Özel, F., & Freire, P. 2016, ARA&A, 54, 401
Page, D. 2016, NSCool: Neutron star cooling code, Astrophysics Source Code Library, ascl:1609.009
Page, D., Beznogov, M. V., Garibay, I., et al. 2020, ApJ, 898, 125
Page, D., Geppert, U., & Weber, F. 2006, NuPhA, 777, 497
Page, D., Lattimer, J. M., Prakash, M., & Steiner, A. W. 2004, ApJS, 155, 623
Page, D., Lattimer, J. M., Prakash, M., & Steiner, A. W. 2009, ApJ, 707, 1131
Page, D., Prakash, M., Lattimer, J. M., & Steiner, A. W. 2011, PhRvL, 106, 081101
Park, S., Zhekov, S. A., Burrows, D. N., et al. 2006, ApJ, 646, 1001
Potekhin, A. Y., Chabrier, G., & Yakovlev, D. G. 1997, A&A, 323, 415
Reed, B. T., Fattoyev, F. J., Horowitz, C. J., & Piekarewicz, J. 2021, PhRvL, 126, 172503
Reinhard, P.-G., Roca-Maza, X., & Nazarewicz, W. 2022, arXiv:2206.03134
Richardson, W. H. 1972, JOSA, 62, 55
Rogers, F. J., Swenson, F. J., & Iglesias, C. A. 1996, ApJ, 456, 902
Sales, T., Lourenço, O., Dutra, M., & Negreiros, R. 2020, A&A, 642, A42
Saumon, D., Chabrier, G., & van Horn, H. M. 1995, ApJS, 99, 713
Schwarz, G. J., Ness, J.-U., Osborne, J. P., et al. 2011, ApJS, 197, 31
Sedrakian, A., & Clark, J. W. 2019, EPJA, 55, 167
Shapiro, S. L., & Teukolsky, S. A. 1983, Black Holes, White Dwarfs, and Neutron Stars: The Physics of Compact Objects (New York: Wiley)
Shigeyama, T., Nomoto, K., & Hashimoto, M. 1988, A&A, 196, 141
Shternin, P. S., & Yakovlev, D. G. 2008, AstL, 34, 675
Shternin, P. S., Yakovlev, D. G., Heinke, C. O., Ho, W. C. G., & Patnaude, D. J. 2011, MNRAS, 412, L108
Socrates, A., Blaes, O., Hungerford, A., & Fryer, C. L. 2005, ApJ, 632, 531
Sotani, H., & Dohi, A. 2022, PhRvD, 105, 023007
Sotani, H., Nishimura, N., & Naito, T. 2022, PTEP, 2022, 041D01
Sugerman, B. E. K., Crotts, A. P. S., Kunkel, W. E., Heathcote, S. R., & Lawrence, S. S. 2005, ApJS, 159, 60
Tajima, H., Hatsuda, T., van Wyk, P., & Ohashi, Y. 2019, NatSR, 9, 18477
Takatsuka, T. 1984, PThPh, 71, 1432
Tamborra, I., Hanke, F., Janka, H.-T., et al. 2014, ApJ, 792, 96
The Lynx Team 2018, arXiv:1809.09642
Urushibata, T., Takahashi, K., Umeda, H., & Yoshida, T. 2018, MNRAS, 473, L101
Utrobin, V. P., Wongwathanarat, A., Janka, H. T., et al. 2019, A&A, 624, A116
Wambach, J., Ainsworth, T. L., & Pines, D. 1993, NuPhA, 555, 128
Wijngaarden, M. J. P., Ho, W. C. G., Chang, P., et al. 2019, MNRAS, 484, 974
Williams, T., & Kelley, C. 2022, Gnuplot 5: an interactive plotting program54, v5.4
Wongwathanarat, A., Janka, H. T., & Müller, E. 2013, A&A, 552, A126
Woosley, S. E. 1987, in IAU Symp. 125, The Origin and Evolution of Neutron Stars, ed. D. J. Helfand & J. H. Huang (Dordrecht: Reidel), 255
Woosley, S. E. 1988, ApJ, 330, 218
Yakovlev, D. G., Kaminker, A. D., & Levenfish, K. P. 1999, A&A, 343, 650
Yakovlev, D. G., & Levenfish, K. P. 1995, A&A, 297, 717
Yakovlev, D. G., & Pethick, C. J. 2004, ARA&A, 42, 169
Zubko, V. G., Mennella, V., Colangeli, L., & Bussoletti, E. 1996, MNRAS, 282, 1321